Subsystem Support Feasibility for Formation Flight Measuring Bi-Directional Reflectance

Sreeja Nag
Massachusetts Institute of Technology
Cambridge, MA 02139
Email: sreeja_n@mit.edu

Kerri Cahoy
Massachusetts Institute of Technology
Cambridge, MA 02139
kcahoy@mit.edu

Olivier de Weck
Massachusetts Institute of Technology
Cambridge, MA 02139
Email: deweck@mit.edu

Abstract— Distributed Spacecraft Missions can be used to improve science performance in earth remote sensing by increasing the sampling in one or more of five dimensions: spatial, temporal, angular, spectral and radiometric. This paper identifies a gap in the angular sampling abilities of traditional monolithic spacecraft and proposes to address it using small satellite clusters in formation flight. The angular performance metric chosen to be Bi-directional Reflectance Distribution Function (BRDF), which describes the directional and spectral variation of reflectance of a surface element at any time instant. Current monolithic spacecraft sensors estimate it by virtue of their large swath (e.g. MODIS, POLDER), multiple forward and aft sensors (e.g. MISR, ATSR) and autonomous maneuverability (e.g. CHRIS, SPECTRA). However, their planes of measurement and angular coverage are limited. This study evaluates the technical feasibility of using clusters of nanosatellites in formation flight, each with a VNIR (visible and near infra-red) imaging spectrometer, to make multi-spectral reflectance measurements of a ground target, at different zenith and azimuthal angles simultaneously. Feasibility is verified for the following mission critical, inter-dependent modules that need to be customized to fit specific angular and spectral requirements: cluster geometry (and global orbits), guidance, navigation and control systems (GNC), payload, onboard processing and communication. Simulations using an integrated systems engineering and science evaluation tool indicate initial feasibility of all listed subsystems.

Table of Contents

1. Introduction

Distributed Spacecraft Missions (DSMs), or space missions using multiple spacecraft with a common goal, have been gaining momentum in the last few decades owing to their ability to improve spatial and temporal performance and reduced risk through increased 'ilities'. DSMs are prohibitively expensive unless small spacecraft are used such that many can be developed and deployed at or less than the cost of one. Cost, schedule and risk considerations in monolithic and distributed missions have ushered in an era of small satellites to complement flagship missions in the important field of earth observation and remote sensing[1]. Nanosatellites (<10kg), now also known as the CubeSat class of satellites, are convenient small satellites to demonstrate better and cheaper performance because they have additional advantages of access to a standard CubeSat bus and secondary payload launches.

We identify multi-angular, multi-spectral[2] (MA-MS) earth observation as an important remote sensing goal that can be best solved using DSMs. MA-MS observations in the solar spectrum are quantitatively best captured using uncertainties in bi-directional reflectance, which will be our major science metric. This paper leverages an integrated systems engineering and science valuation tool to design the subsystems in keeping with science traceability, technological constraints and subsystem interdependencies. Specifically, we demonstrate the technical feasibility of the DSM concept (using some baseline architectures) in terms of the supporting subsystems that will be critical to such a mission. The framework can select the optimal architectures that maximize multi-angular science performance for minimum resources, within technological COTS feasibility.

2. Multi-Angular Remote Sensing

In earth science remote sensing, DSMs can be efficient in directly improving sampling in three out of five dimensions of an observed image – *spatial, temporal, angular, spectral and radiometric*[3]. DSMs encompass a diverse family of spacecraft configurations. They include homogenous constellations such as Global Positioning System, heterogeneous constellations such as the A-Train, close proximity clusters in formation flight such as Edison and fractionated spacecraft where all physical entities share subsystem functions such as System F6.

Challenges with Current Measurements
Angular sampling implies taking images of the same ground spot at multiple 3D angles of solar incidence and reflection

simultaneously. The near-simultaneous measurement requirement deems monoliths insufficient for accurate and dense angular sampling (Figure 1). Monolithic spacecraft have traditionally approximated the angular samples by combining measurements taken over time with forward-aft (e.g. TERRA's MISR[4]) or cross-track swath (e.g. TERRA's MODIS[5]) sensors. However, a single satellite can make measurements only along a restrictive plane with respect to the solar phase and most earth observation satellites are even more restricted since they are on sun-synchronous orbits. Further, the angular measurements are separated in time by many minutes along-track or weeks cross-track. In areas of fast changing surface/cloud conditions especially during the melt season/tropical storms, a few days can make a big difference in reflectance.
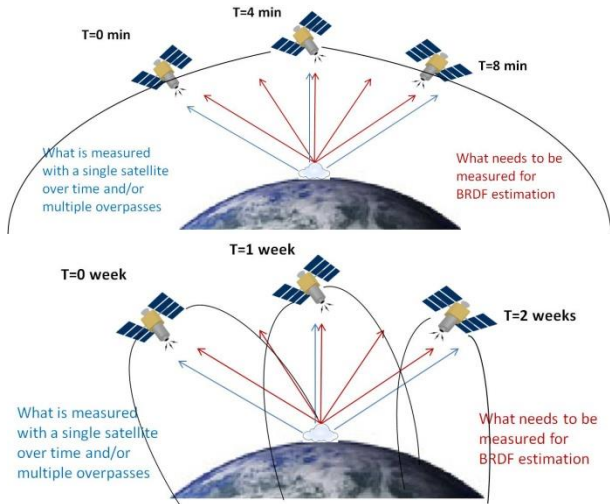

Figure 1: Measurements a single satellite is capable of making, in blue, versus multiple angular sampling measurements in red. 'T', ranging over a few minutes for forward-aft sensors (top panel) or over a few weeks for cross-track sensors (bottom panel), represents nominal time differences that a LEO satellite takes to make the given measurements.

The widely accepted metric to quantify the angular dependence of remotely sensed signal is called BRDF or Bidirectional reflectance-distribution function. BRDF of an optically thick body is a property of the surface material and its roughness. It is the ratio of reflected radiance to incident irradiance that depends on 3D geometry of incident and reflected elementary beams[6]. At any given wavelength, it depends on four major angles – the solar zenith (SZA) and azimuth angle (SAZ) and the view zenith (VZA) and azimuth angle (VAZ). The azimuth angles are simplified to one angle called the relative azimuth angle (RAZ).

To name a few applications, BRDF is used for the derivation of surface albedo, calculation of radiative forcing, land cover classification, cloud detection, atmospheric corrections, and aerosol optical properties[7]. Accurate BRDF time series at customized spectra and spatial scales can estimate many biophysical phenomena that are currently wrought with errors. For example, up to 90% of the errors in the computation of atmospheric radiative forcing, which is a

key assessor of climate change, is attributed to the lack of good angular description of reflected solar flux[8]. MODIS albedo retrievals show errors up to 15% due to its angular and spatial under sampling when compared to CAR. Gross Ecosystem Productivity (GEP) estimations, to quantify sinks for anthropogenic CO_2, show uncertainties up to 40% and usage of CHRIS angular data has shown to bring them down to 10%[9]. Accuracy and frequency of BRDF estimation is therefore a representative metric of the 'goodness' of all sampling dimensions discussed previously.

Table 1: Comparison of current space borne mission instruments with BRDF products (rows) in terms of BRDF measurement metrics (columns). Red highlights indicate sparse measurements for BRDF estimation.

BRDF-Science → Metrics Current Instruments ↓	Number of angles	Ground Pixel Size in km X km	Revisit Time (any view) in days	Spectral Range	# of spectral bands
[1]MODIS	1	0.25 to 1	~2(16 day RGT)	0.4-14.4 μm	36
[1]POLDER	14	6 X 7	~2(16 day RGT)	0.42-0.9 μm	9
[1]CERES	1	10 to 20	~2(16 day RGT)	0.3-12 μm	3
[2]MISR	9	0.275 to 1.1	9(16 day RGT)	0.44-0.87 μm	4
[2]ATSR	2	1 to 2	3-4	0.55–12 μm	7
[2]ASTER	2	0.015 to 0.09	~2(16 day RGT)	0.52–11.65 μm	14
[3]CHRIS	5-15	0.017 to 0.5	As per command	0.415-1.05 μm	18-63

Airborne instruments estimate local BRDF very accurately because they are able to fly around a ground spot taking thousands of angular measurements. NASA's heritage airborne BRDF instrument is called the Cloud Absorption Radiometer[10] (CAR), developed at Goddard Space Flight Centre (GSFC), has 14 channels of bandwidth 6-40 nm, makes up to 114600 directional measurements of radiance per channel per aircraft circle at a spatial resolution of 10-270 m[10]. However, these measurements cannot be scaled up globally or repeated temporally.

Spacecraft can only approximate BRDF to varying degrees of inaccuracy (Figure 1). Their instruments, as shown in Table 1, estimate BRDF by making multi-angular measurements owing to their large cross track swath[1] (e.g. MODIS[5], POLDER[11],CERES[12]), multiple forward and aft sensors[2] (e.g. MISR[4],ATSR[13],ASTER[14]), or autonomous maneuverability to point at specific ground targets that they have been commanded to observe[3] (e.g. CHRIS[15]). Other than CHRIS (which does not provide global or repeatable coverage) and POLDER (with very coarse spatial resolution), none of the instruments provide full 3D angular coverage within a short time frame. MISR is also limited in resolution of the solar spectra and does not measure in the photosynthetic region.

Proposing a new Measurement Solution
Near-simultaneous angular sampling can be improved by using a cluster or constellation of nanosatellites on a repeating-ground-track orbit[16]. The cluster can make multi-spectral measurements of a ground spot at multiple 3D angles at the same time as they pass overhead either using narrow field of view (NFOV) instruments in controlled formation flight (Figure 2-a) or wide field of view (WFOV) instruments with overlapping ground spots providing

integrated images at various angles (Figure 2-b). The mission will not only need precise relative formation flight but also strict attitude control, orbit maintenance, onboard processing for the multi-spectral data, inter-satellite calibration and a good communication channel to downlink the collected data. Parallel studies have demonstrated availability of feasible orbits and their performance trade-offs[3], payload development [17] to support such a mission, science models to quantify the performance of such DSMs[2],[12],[13] as well as open-source flight software to continually update satellite capability for staged, scalable deployment[20]. This paper focuses on quantitative methods to evaluate such a mission's development and operational feasibility within achievable COTS (Commercial Off-The-Shelf) technologies identified in Reference[21], satellite vendor websites and mission-tested components.
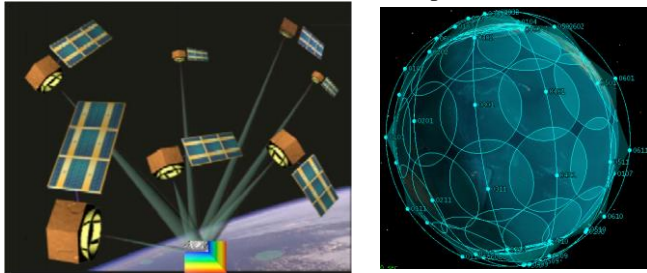

Figure 2: DSMs making multi-angular, multi-spectral measurements by virtue of (left) pointing its NFOVs at the same ground spot, as it orbits the Earth as a single system (adapted from Leonardo BRDF[22]), or (right) their overlapping WFOVs at different angles.

3. FEASIBILITY EVALUATION METHODS

The framework to assess the optimal formation architectures (unique combination of design variables such as orbit parameters, payload FOV, imaging mode, etc.) and validate their BRDF estimation capabilities couples a systems engineering model (SysEng) with a science evaluation model (SciEval) [11]. SysEng is driven by Model-Based Systems Engineering (MBSE) while SciEval by Observing System Simulation Experiments (OSSE). A tradespace of formation architectures can be analyzed by varying the design variables in the MBSE model and assessing its effect on data assimilation and science products using OSSEs, per time step (Box II) and then for an extended period within mission lifetime (Box I) as shown in Figure 3. The full system will take measurement requirements (e.g. angular and spatial sampling), technology constraints (e.g. maximum mass, highest altitude) and biomes of interest (e.g. vegetation, deserts) as input and produce three outputs: science metrics (e.g. BRDF error), lifecycle cost and extent to which technology constraints were met. Biomes are large naturally occurring communities of flora and fauna occupying major habitat. They have very different BRDF and therefore may need different cluster designs to image.

Systems Engineering Model
The systems engineering model is shown in the top blue Box IIIa in the innermost layer in Figure 3. SysEng contains

the following modules - shown in Figure 4 - as an N2 diagram: orbits and imaging modes, guidance, navigation and control systems (GNC), payload, onboard processing, communication, propulsion and cost. The subsystem modules identified are critical for the mission and need special customization. For example, power has been top out because there are no special power requirements over the 6U CubeSat standard. The vertical arrows represent inputs and horizontal arrows outputs from the subsystems.

The SysEng model will take BRDF measurement requirements and 6U CubeSat/nano-satellite bus requirements as inputs (as identified in the previous section), use them as constraints to generate hundreds of cluster architectures, and output the following three types of metrics shown in Figure 4: (a) science performance in green (e.g. Signal-to-Noise Ratio or SNR), (b) technology supportability in black, and (c) resource measures in red (e.g. cost). The orbits/modes and payload module are the architecture generators; GNC (guidance, navigation and control with GPS and ADCS), onboard processing, communication and propulsion modules are the architecture evaluators; and the cost module is the architecture sizer. The model also enables optimization within the individual modules to maximize metric values.
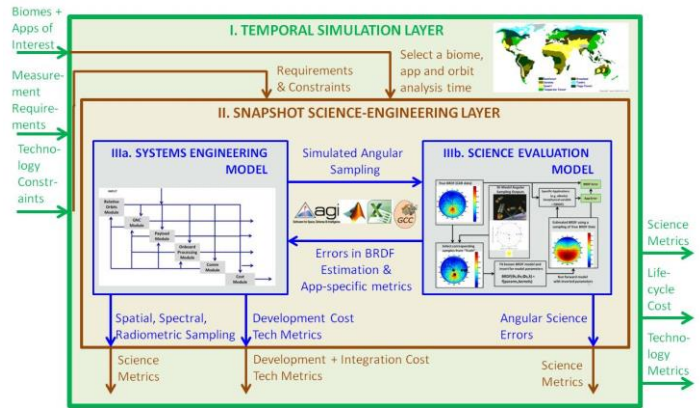

Figure 3: Summary of the overall approach to calculate BRDF science performance, technological requirements and cost of different mission architectures. There are three layers of analysis.

The mission measurement goals are derived from the science goals and the requirements of current, successful space borne instruments and airborne instruments. Measurement zenith angles up to 80°, measurement azimuth up to 360°, and solar zenith angles up to 80° are ideal for the full angular spread. The different strategies for payload pointing for a given set of orbits, to maximize performance, are represented by different imaging modes, as described in Reference [19]. While the orbits module determines how the satellites will be organized in space, the imaging modes dictate where they will point to make optimal images in coordination. Spectral requirements derived from the CAR[10] instrument ask for 14 wavebands with spectral resolution varying from 10-40 nm over the spectral range of 350 and 2300 nm. The payload can be a spectrometer (NFOV) or a radiometer (WFOV), and has been analyzed in
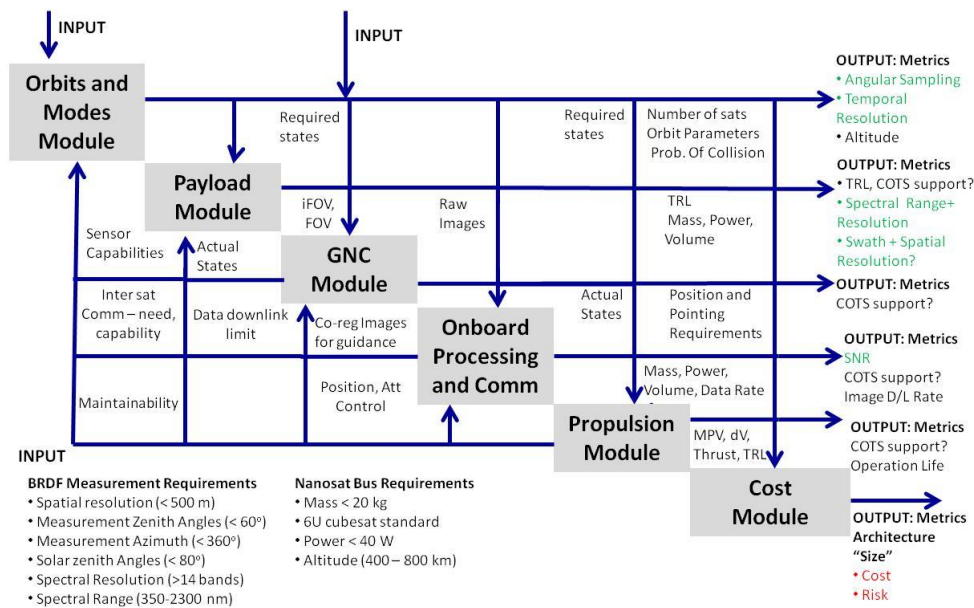
INPUT INPUT

Orbits and Modes Module

OUTPUT: Metrics
• Angular Sampling
• Temporal Resolution
• Altitude

Required states

Payload Module

Required states

Number of sats
Orbit Parameters
Prob. Of Collision

OUTPUT: Metrics
• TRL, COTS support?
• Spectral Range+ Resolution
• Swath + Spatial Resolution?

iFOV, FOV

Raw Images

TRL Mass, Power, Volume

GNC Module

Sensor Capabilities

Actual States

Inter sat Comm − need, capability

Data downlink limit

Co-reg Images for guidance

Onboard Processing and Comm

Actual States

Position and Pointing Requirements

OUTPUT: Metrics
COTS support?

OUTPUT: Metrics
SNR
COTS support?
Image D/L Rate

Maintainability

Position, Att Control

Mass, Power, Volume, Data Rate

Propulsion Module

MPV, dV, Thrust, TRL

OUTPUT: Metrics
COTS support?
Operation Life

Cost Module

INPUT

BRDF Measurement Requirements
• Spatial resolution (< 500 m)
• Measurement Zenith Angles (< 60°)
• Measurement Azimuth (< 360°)
• Solar zenith Angles (< 80°)
• Spectral Resolution (>14 bands)
• Spectral Range (350-2300 nm)

Nanosat Bus Requirements
• Mass < 20 kg
• 6U cubesat standard
• Power < 40 W
• Altitude (400 − 800 km)

OUTPUT: Metrics
Architecture "Size"
• Cost
• Risk

Figure 4: Systems Engineering Model (MBSE-based)

detail in References [17], [18]. A medium spatial resolution of <500 m is considered as an initial requirement. The 500 m resolution condition has been imposed for imaging at the longest wavelength (2300nm), which corresponds to a resolution of 188 km at MISR's highest band. Since MISR's resolution at its highest band (865 nm) is 275m, the intent was to outperform by ~30%. The approach allows this requirement to be customizable, and it will be seen later that spatial resolutions coarser than 500m are preferable to improve swath for more coverage and for allowing more integration time per image, thus more SNR. The altitude range requirements used are 400 km to 800 km (LEO) because that range corresponds to the most common shared rides available with primary payloads[23]. If all the nano-satellites can be launched as the primary payload itself, then the orbit constraints may be removed. The given LEO range has been found to be a sweet spot for payload operations and maintenance against atmospheric drag. The bus requirements are set to: mass less than 20 kg; physical dimensions less than 10X20X30 cm; and power less than 40W, so as to adhere to the expected (albeit optimistic) ~6U CubeSat standards.

Among the outputs on the right side of Figure 4, angular spread serves as the input into SciEval (Box IIIb in Figure 3) because it cannot be evaluated in absolute terms like the other metrics. Only architectures with output values greater than the technology constraints and measurement requirements (Input to BoxI in Figure 3) will be considered. For example, attitude or position determination/control technologies required by the GNC module (e.g. star tracker accuracies) will be checked if they are COTS supported, or if whether the downlink channels for the required data rates can be obtained. If not, either the relevant architectures are discarded, or the measurement requirements are relaxed (e.g. payload collection rate reduced)[21]. [24]

Subsystem Sizing Models
The architecture generating modules, orbits[3] and imaging modes[19] and payload[17] have been described in previous literature. Reference[24] has described the cost sizing modules. Discussed below are some subsystem models that will be used to determine the feasibility of the generated architectures, applied in the next section.

Previous work on precise pointing control in a hardware-in-the-loop (HWIL) simulation was studied. Tests reviewed included the SPHERES Program, GNC system development via MicroMAS [25] and ExoplanetSAT [26], and DSS metric evaluation via the Terrestrial Planet Finder (TPF) program and DARPA System F6, in a bid to develop state-of-art algorithms for MA-EO cluster fight. The reaction wheel stage of ExoplanetSat, both in simulation and HWIL verification on MIT's spherical air bearing testbed, has shown pointing precision at LEO within 40 arcsec [26] or 0.011°. An additional fine pointing stage is expected to increase the pointing precision ten times. MicroMAS's concept of operations (ConOps) have also been tested on the same testbed and the air bearing was able to closely track the commanded angular orientation[27], verifying the existing HWIL control simulation. Blue Canyon's XACT system[1] with star trackers and 3-axis reaction wheels claims to provide up to 0.001^0 of pointing determination and 0.01^0 of control. While XACT has never flown, MIT's Hardware in Loop (HWIL) lab testing[26] has shown up to 0.011^0 of control. In space, CubeSats have demonstrated between 0.5° (BRITE[28]) and 1° (CanX series[29]) with sun sensors and magnetometers.

For the formation and LVLH motion to be intact, the differential orbital elements among all the satellites in the

---

[1] http://bluecanyontech.com/product/xact/

4

cluster must be maintained within error margins. In Low Earth Orbit (LEO), the major disturbances to be accounted for are atmospheric drag and J2 effects due to a non-spherical Earth. If these disturbances act on the different satellite orbits differently, it may cause the orbits to drift apart and eventually break the formation. Atmospheric drag causes the semi major axis and eccentricity of the orbit, and therefore orbit velocity and period, to change. Corrections, if needed, can be provided by propulsion systems aimed at raising the altitude back periodically, either by continuously providing the ΔV lost or using Hohmann transfer every few weeks to correct for the Δa. J2 effects cause a satellite's right ascension of ascending node (RAAN) to rotate by the amount given in Eq.(1) in degrees per day. Corrections need a large ΔV because they effectively imply a plane change at orbital velocities[30]. Equatorial orbits need less fuel for the plane change than polar orbits. Alternatively, missions are designed to account for or even take advantage of the rotation (e.g. sun-synchronicity). J2 also causes rotation of the argument of perigee, however since this thesis looks at only those solutions with circular orbits, those equations have not been modeled.

$$\Delta\Omega = -1.5nJ_2(Re/a)^2(\cos i)(1-e^2)^{-2}$$
$$\cos\Delta\theta = (\cos i)^2 + (\sin i)^2 \cos\Delta\Omega$$
$$\Delta V = 2V\sin\Delta\theta/2$$

(1)

The above equations are valid only for impulsive propulsion such are chemical or cold gas propulsion. Electric propulsion provides an alternative solution. Its high specific velocity (Isp) and low thrust require longer times and larger ΔV, however, they may correspond to lower fuel mass at the cost of power. When using electric propulsion, the required ΔV for plane changes or altitude changes is calculated using the Edelbaum equations[31], [32], simplified for this paper. V1 and V2 are the initial and final orbital velocities, and $\Delta\Omega$ is the required plane change. The time to complete the maneuver is then calculated from the ΔV, depending on the input power to the thruster (P) and efficiency (ε) – from (3). Mf and Mi are the final (wet) and initial masses of the spacecraft from the standard rocket equation.

$$\vartheta = \tan^{-1}\left[\frac{\sin\left(\frac{\pi}{2}\Delta\Omega\right)}{V1/V2 - \cos\left(\frac{\pi}{2}\Delta\Omega\right)}\right]$$
$$\Delta V = V1 * \cos\vartheta - V1 * \frac{\sin\vartheta}{\tan\left(\frac{\pi}{2}\Delta\Omega + \vartheta\right)}$$

(2)

$$T = 2 * \varepsilon * P/g * Isp$$
$$Mf = Mi * \exp\left[\frac{\Delta V}{g * Isp}\right]$$
$$time = \Delta V * Mf/T$$

(3)

The cluster's imaging modes are supported by the attitude determination and control stems (ADCS), housed under the GNC (guidance navigation and control) module in the Systems Engineering model. Depending on the mode, the satellites will need to constantly change their initial attitude, as defined in their body-fixed reference system, in order to point their payload toward the ground target, as defined in the geocentric equatorial reference system (IJK)[33]. An intermediate reference frame, called the orbital or LVLH frame, is a useful transition between the above two. The orientation of a satellite in the LVLH frame is defined by a 4D vector called a quaternion, which maps the satellite attitude in the body frame to its attitude in the LVLH frame. It consists of a three-element hyper-imaginary vector part and a single-element scalar part: $\bar{q} = q_1\hat{\imath} + q_2\hat{\jmath} + q_3\hat{k} + q_4$, where the quantities $\hat{\imath}$, $\hat{\jmath}$, $\hat{k}$ follow a set of rules analogous to the single-dimension imaginary number $i = \sqrt{-1}$, and similar in form to the rules for forming cross products. The real coefficients of the quaternion components may be expressed in vector notation as $q = [q_1\ q_2\ q_3\ q_4]^T$. Given a rigid-body rotation of angle θ about the axis, $\hat{n}$, expressed in some reference frame, the resulting orientation given by unit vector of the body may be characterized as below. The inverse of a quaternion may be found simply by changing the sign on the vector part.

$$q = \begin{bmatrix} q \\ q_4 \end{bmatrix} = \begin{bmatrix} \hat{n}\sin\left(\frac{\theta}{2}\right) \\ \cos\left(\frac{\theta}{2}\right) \end{bmatrix} = [q_1\ q_2\ q_3\ q_4]^T$$

(4)

Equation (4) can be used to calculate required attitude states, given an imaging mode and cluster satellite states, as will be shown later in the results. A separate set of quaternions for orienting the satellites from the LVLH reference to the inertial IJK frame is needed to ensure any extra control that continuous Earth pointing may require. Up to an additional $0.06°$ per second of slewing per satellite, also known as the yaw-pitch maneuver, is needed for continuously orienting the HCW or LVLH frame's X axis toward the Earth Center (IJK). Given the required nadir angle (η) and azimuth angle(Φ) attitude, attitude errors ($\Delta\Phi$ in azimuth and $\Delta\eta$ in nadir), position errors (ΔI in-track or IT, ΔC cross-track or CT, Rs radial or R), earth radius Re and orbit altitude h, the magnitude of mapping error in the respective directions can be calculated by the following equations[34] in kilometers:

$$\text{Azimuth Error} = \Delta\Phi*D*\sin\eta$$
$$\text{Nadir error} = \Delta\Phi*D/\sin\varepsilon$$
$$\text{IT error} = \Delta I\frac{Re}{Re+h}\cos\text{asin}(sin\lambda\ sin\phi)$$
$$\text{CT error} = \Delta C\frac{Re}{Re+h}\cos\text{asin}(sin\lambda\ cos\phi)$$
$$\text{R error} = \Delta Rs*\sin\eta\ /\sin\varepsilon$$

(5)

Elevation of any satellite (ε), Earth central angle (λ), length (Lf) and breadth (Wf) of an elliptical footprint due to an angular conical beam of width FOV can be obtained from basic geometry[34].

$$Lf = D\sin FOV/\sin\varepsilon$$
$$Wf = D\sin FOV$$
$$\lambda = 90 - \eta - \varepsilon$$
$$\varepsilon = \cos^{-1}\frac{\sin(\eta)}{\sin(\rho)}; \rho = \sin^{-1}\frac{Re}{Re+h}$$

(6)

The communication module has not been explored with link budget equations, since standard LEO parts will be required as long as the required data rates can be supported. The trade-offs between direct downlink from all satellites and inter-sat data transfer has been briefly analyzed. For any pair of satellites separated in RAAN ($\Delta\Omega$) and true anomaly Δm, the maximum (λ_{max}) and minimum (λ_{min}) earth angle (λ) can be found from [35]:

$$\cos \lambda_{max} = cos^2(\Delta f/2) \cos \beta - sin^2(\Delta f/2)$$
$$\cos \lambda_{min} = cos^2(\Delta f/2) - sin^2(\Delta f/2) \cos \beta$$
$$\cos \beta = cos^2 i + sin^2 i \cos \Delta\Omega$$
$$\Delta f = \Delta m - 2 tan^{-1}[-tan(\Delta\Omega/2) \cos i]$$

$$(7)$$
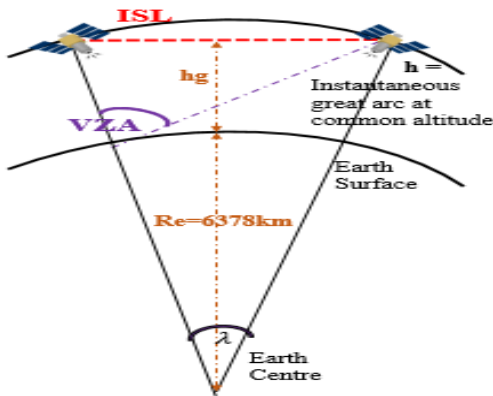
Figure 5: Representation of the geometry used to calculate view zenith angle (VZA) and inter-satellite link (ISL) between two spacecraft at altitude h.

Given the chief orbit altitude h, the maximum and minimum separations between satellite pairs and the angles they subtend on the ground can be easily calculated. The satellites can be cross-linked if the subtended earth angles are less than $\lambda = \lambda_c$ in the equation below, derived from the geometry in Figure 5 and validated against Reference[35], for a minimum cross-linking altitude of h_g.

$$\cos \frac{\lambda_c}{2} = \frac{Re + h_g}{Re + h}$$

$$(8)$$

It is obvious from Figure 5 that greater inter-satellite distances or ISL (worse from communication) leads to greater view zenith angles (better for angular imaging). Instantaneous VZA is calculated as the angle subtended under one satellite by another while λ as the angle subtended at the Earth centre by both satellites. From geometry and the trigonometric sine law, VZA, h and ISL are related as[3]:

$$\sin x \cot VZA + cos x = h/ISL$$
$$ISL * \sin x = (Re + h) * \sin \lambda$$

$$(9)$$

If the satellites in question are not in the same orbit, the great arc joining them at their common altitude is used for the calculations. Relative azimuth angle (RAZ) with respect to the sun will be calculated depending on the instantaneous orientation of this great arc plane with respect to the Sun.

A large number of satellites in a cluster performing 3D imaging is expected to generate a large amount of data. The data need to be processed onboard, compressed and/or down-linked. NASA Jet Propulsion Laboratory has demonstrated a 50 Mbps downlink from the International Space Station (OPALS) over 148 seconds[36]. The Aerospace Corporation is currently building a 3U CubeSat (OCSD) to demonstrate the same optical downlink rate [37]. NASA JPL is also looking to test its Ka-band downlink capability on its ISARA cubeSat and demonstrate up to 100 Mbps of data rate[38]. JPL is also developing Ka-band parabolic deployable antennas (KaPDA) to achieve a 0.5m dish in space[39]. Beam divergences exiting the telescope were on the order of 0.02-0.1° for both beams, which are difficult to achieve using standard ADCS systems for nanosatellites. However, recent developments are ushering in improvement. University of Toronto's BRITE constellation has flown 10 arcsec of determination and ~0.5° of control[28]. MIT has tested a CubeSat optical transmitter that can achieve at least 10 Mbps, with a fine steering ADCS capable of 3σ errors better than 0.012°[40]. band capabilities go from 50 Mbps within 0.5 kg/10 W/TRL 6 by Syrlinks, France[2] to 400 Mbps within 4 kg/75 W/TRL 9 by L3 Cincinnati Electronics[3]. X, Ka band or optical communication thus provides an optimistic option to retrieve data from the nano-satellite clusters. NASA ARC's Edison program (to launch in 2015) plans to demonstrate Inter-Sat Links (ISL) and the above downlink strategy among 8 1.5U CubeSats [41].

The onboard processing unit is primarily used to reduce data onboard before downlink. An example of a standardized COTS unit for onboard processing is NASA GSFC's SpaceCube Mini - a modular processing unit. The design has been built off the GSFC expertise in designing the legacy SpaceCube 1 that flew on the Hubble Servicing Mission and the ISS MISSE7 experiment[42]. It physically conforms to the volume requirements of a standard 1U (10cm x 10cm x 10cm) CubeSat and incorporates the Xilinx Virtex-5, a high speed, high density, radiation tolerant FPGA design. Built in peripherals include 512Mx16 of SDRAM, 96 GB of flash memory, a radiation hard Aeroflex FPGA, a 12 bit analog to digital converter, and local power regulation. The GSFC SpaceCube MINI design also includes one expansion slot to add in an optional user I/O card, thus making it easily integrable with the developed GNC software at MIT and any other mission unique I/O software. SpaceCube is being used within the Intelligent Payload Experiment (IPEX), a CubeSat that launched in December 2013 to validate autonomous processing and product generation for the Hyperspectral Infra-red Imager (HyspIRI) mission concept[43]. It has demonstrated high fidelity operations models and hyperspectral image processing, both of which are required for BRDF DSM. SpaceCube 2.0's SAR Nadir Altimetry application has

shown a 6:1 reduction in downlink data by moving first stage ground operations on-board, to make cluster science data manageable. COTS propulsion modules available for nano-satellites could be cold gas thrusters [44] or electrospray thrusters [45] (which are not yet ready for flight). A commercial company called AustinSat[4] manufactures 3D printed CG thrusters with 6DOF and an easily scalable propulsion tank where 1U of propellant provides 40 m/s of ΔV.

4. RESULTS ON SUBSYSTEM FEASIBILITY

This section will use the known modeling procedures (pre-phase A level only) for the mentioned critical subsystems to show that the generated architectures that maximize science performance are feasible. Feasibility will be established for a few but representative baseline architectures and extrapolations will be drawn for the others. The concept of operations for the mission is to collect multi-angular images by pointing sensors at the same local ground spot at the same time during orbit day; and perform calibration, downlink and maintenance during orbit night. Occasional (expected every 3-4 days) overpasses will also be used to inform all the satellites about the current and predicted positions of the others. Possibility of more autonomy, de-orbiting and pointing strategies are described in [19].

Position and Attitude Determination and Control
Attitude determination is of great importance for all modes because of the co-pointing requirement for near-simultaneous measurement at the same ground spot. To increase overlap of ground spots, multi-spectral snapshot imagers for 2D spatial imaging can be used. The feasibility of such a system on nanosatellites has been demonstrated in simulation[17] using currently available spectral elements like tunable filters and waveguides. For a 1024X1024 pixel CCD focal plane and a ground sampling of 500m, pointing accuracy of 0.03^0 is needed to stay within one pixel of error. Using the technology literature from the previous section, this section will show the deterioration in image size with increasing pointing errors and demonstrate that acceptable performance is possible even with the ADCS control jitter of 0.5°. Position errors up to 2 km have been considered, which have been demonstrated using GPS (e.g. RAX[46]).

Table 2: RAAN and TA in deg, in the form of osculating Keplerian elements, for 4 satellites in a cluster when arranged in 2 baseline (B/L) configurations [23],[25]. The other Keplerian elements are the same for all satellites, a = 6378+650 km, i = 51.6º, ω = 0, e= 0.

Worst B/L	0::0	0::-5	-5::-1	5::-4
Best B/L	0::0	0::-5	-5::-6	5::-4

Attitude control analysis on the 4-satellite baseline configurations is performed in the LVLH frame, by adapting the analemma equations[3], and later mapped to the IJK

[4] http://austinsat.net/cold-gas-thruster-for-cubesats/

frame. The equations represent the movement of satellites with respect to a chosen reference satellite, when the only difference between their orbits is differential RAAN and TA[3]. They are used for baseline analysis because they have been shown to provide required science performance by using appropriate imaging modes[19]. The best and worst configurations of 4 satellites each, from the baseline analysis[16], [19] are plotted in Figure 6 with Keplerian elements from Table 2.
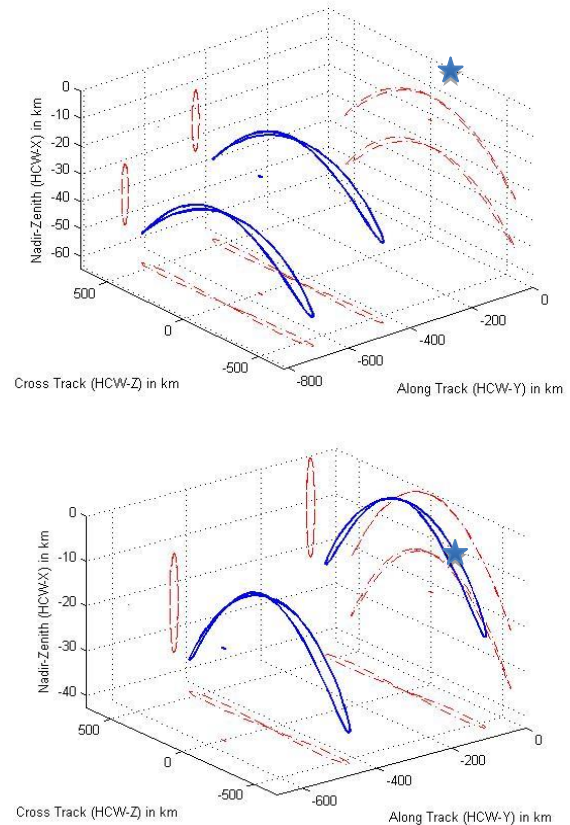

Figure 6: LVLH curves (blue) and their projections (red) over one orbit for a 4 satellite cluster with Table 2's configuration (top: Best, bottom: Worst), where LVLH patters are calculated by the analemma equations. The reference satellite, at the blue star, looks nadir.

Figure 6 shows the relative motion in the LVLH frame of Satellites 2, 3, 4 with respect to the base satellite (blue star at origin) in two baseline configurations from [16], recounted again in Table 2. These configurations correspond to maximum (worst) and minimum (best) errors, in terms of science evaluation, assuming the reference satellite looking down. The orbits of all satellites in both configurations, except Satellite #3, are the same. Differential RAAN (Ω_R) causes the cross-track motion while differential TA (θ_k) causes a constant offset. Better performance is seen from more offset and more cross-track coverage. The dynamic measurement zenith (top) and azimuth (bottom) angle subtended at the ground target by each satellite is seen in Figure 6 for the best (continuous line) and worst performing (triangular markers) baseline configurations with 4 satellites each. Each plot should thus have 4 * 2 = 8 curves for the

angles subtended by 4 satellites in 2 different configurations. However, since 3 of 4 satellites have the same orbit, their curves in Figure 6 are overlapped. Only Satellite #3 (blue) shows different curves.
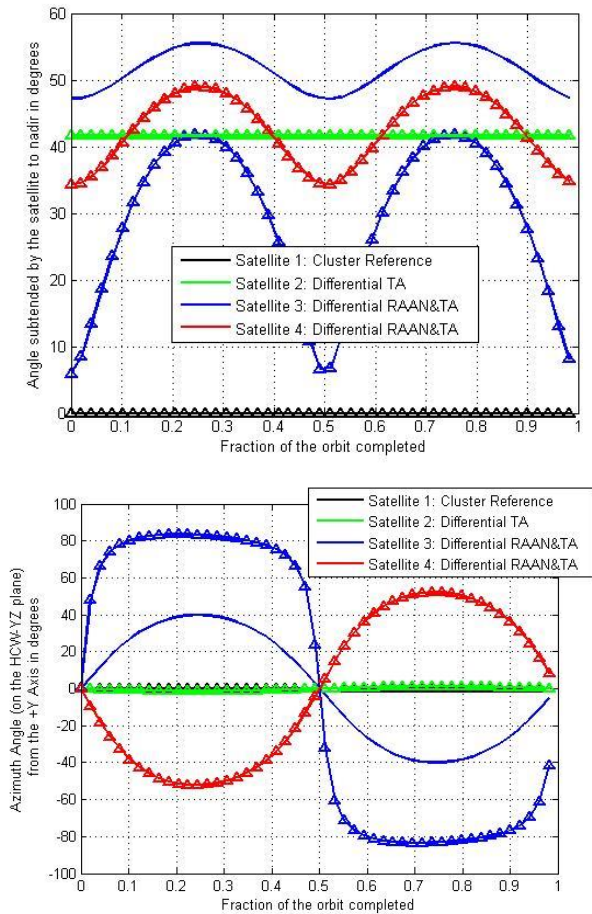

Earth, or for making sure that the LVLH-X axis remains pointing toward the Earth center. Since this additional control for yaw-pitch maneuvering is an order of magnitude more than the required control for LVLH co-pointing, it has been decoupled to emphasize the impact of cluster architecture on the latter.

*Overlapping Ground Spots—*The ability to control the cluster such that all satellites co-point to the same ground spot simultaneously, irrespective of orbit or imaging mode, is a critical enabler of mission science. The overlapping ground spots of all satellites in the cluster produce a multi-angular image. Assuming conical fields of view (FOV), the ground spot of the nadir-looking satellite will be circular with a radius of h*tan(FOV/2). The ground spot of all other satellites will be ellipses whose heel-toes are oriented in the azimuthal direction, and size given by Equation (6). I assume that the full circle or ellipse fits within the square (with sharp or rounded corners) FPA such that the shown ground spot overlap corresponds to the overlap of the processed images. A square FPA was assumed to reduce the constraints on the ADCS system. A rectangular FPA can improve the percentage of FPA pixels used to image an ellipse, however we will need to control the roll about the payload pointing axis so that the great axis of the ground spot ellipse is imaged on the FPA long side.

Figure 7: [Top] View zenith (VZA) and [Bottom] azimuth angle (RAZ) at the ground target under the reference satellite as sampled by the 4 satellites (different colors), in the best (continuous line) and worst (triangular markers) case baseline configurations. All angles are in LVLH frame.

All angles are measurable because of the assumed ±60° slewing ability for the XACT and other commercial systems. Large VZA provided by satellite 3 and the symmetric azimuthal coverage achieved by satellite 3 and 4 in best case configuration causes the configuration to perform better than the worst case configuration. These nadir and azimuth angle outputs per satellite per time step are used as inputs for analyzing the effects of attitude control error and slew requirements. The VZA and RAZ curves for each satellite in any cluster configuration serve as angular requirements. The RAZ curves will be added to the solar azimuth bias, depending on the orientation (beta angle) of the chief orbit, to obtain the IJK RAZ requirement. They inform the quaternion that maps the spacecraft body frame (containing a fixed payload) to the LVLH frame. Additional control is needed for every satellite to point toward the
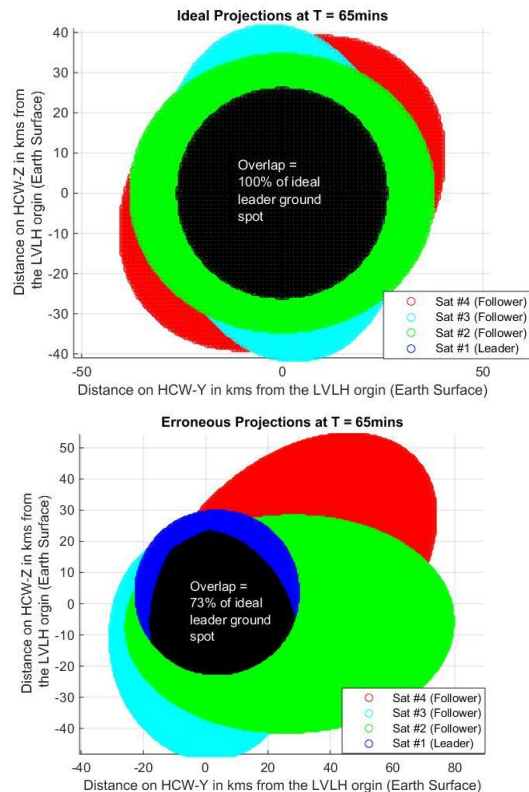

Figure 8: Ground spot overlap for the Worst B/L cluster in Table 2, ideally (top) and with a 1 deg attitude error and 4 km position error (bottom) for all satellites. The projects are for one instant of time, 67% into the orbital period. Flat Earth assumed.

The circle and ellipses will change shape, orientation and position depending on attitude and position errors. Assuming the attitude error in the nadir and azimuth direction are $\Delta\eta$ and $\Delta\Phi$, the pointing error in the nadir direction is the same while that in the azimuthal direction is scaled ($\Delta\Phi*\sin\eta$). The projected ellipse orientation rotates by the latter amount due to these errors. Assuming errors of ΔI, ΔC and ΔR in the in-track, cross-track and radial directions, the resulting mapping errors are given by Eq. (5) and (6). A new nadir angle per satellite, per time step can be found by adding the pointing error to the ideal, and the ground projection ellipse length and width recalculated from (6). The center of the ellipse shifts from the LVLH center by an amount given by (10) and errors are calculated from (5).

$$\alpha = \text{IT err} + \text{Nadir err} * \cos\Phi + \text{Azim err} * \sin\Phi$$
$$\beta = \text{CT error} + \text{Nadir err} * \cos\Phi - \text{Azim err} * \sin\Phi$$
$$\textbf{(10)}$$

The ideal overlap of ground spots for the 4-sat worst baseline cluster in Table 2 at the 65th minute, or 67% onto its orbit, is seen in Figure 8-top. A flat earth is assumed, for simplicity and because Earth curvature introduces little difference in the overlap results for a reference satellite with a <20 km ground spot. The overlap between the ground spots is a perfect circle that covers 100% of the ground pixels of the reference or leader satellite. Assuming 1 deg of attitude error (demonstrated on CanX[29]) and 2 km of position error (demonstrated on RAX[46]), the erroneous overlap between the ground spot at the same time is shown in Figure 8-right. The shifted spots reduce the overlap to 73% of the ground pixels of the leader satellite. A constant position error shows no effect on ground spot overlap (affected only by relative changes).
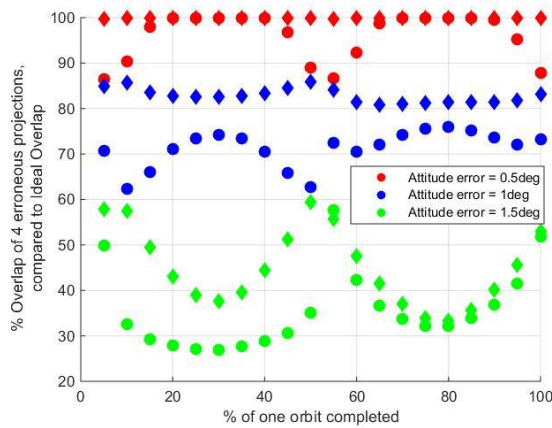

Figure 9: Percentage overlap among the ground spots of 4 satellites in the best (diamonds) and worst (circles) B/L configuration in Table 2. Position (2km for all) and attitude errors (by color) are assumed as a constant bias. Flat Earth assumed.

Random and different position errors per satellite cause a ground overlap change, but effects of <2 km position errors are small compared to <1 deg attitude errors. Further, it is far cheaper to reduce that position error than the attitude

error on CubeSats. The effect of increasing constant attitude error on all satellites on the percentage overlap of their ground spots over a full orbit is shown in Figure 9, for both cluster configurations in Table 2. The best baseline cluster is less affected by the attitude error. Less than 1 degree errors result in better than 50% overlap, irrespective of configuration. If attitude control like BRITE[28] is possible, overlaps are better than 90%, indicating successful co-pointing. When attitude errors are modeled as Gaussian distributions instead of a constant bias (Figure 10), a 1σ error of 0.5° when inputted into 100 Monte Carlo (MC) runs result in ~30% instances of the ground spot overlap greater than 98% and negligible instances of less than 60% overlap. Since multi-angular images and BRDF need co-pointing, greater than 1° errors will generate large amounts of useless data due to less than 50% ground spot overlaps.

ADCS is the most critical enabler of the imaging modes, or to point the payloads coherently[19]. Mode #1 requires the same satellite to point downward and the others to point below the leader satellite. Mode #2 is similar, however the leader satellite dynamically changes, as determined by the ground stations by maximizing expected science. Mode #3 requires all satellites to track a few, pre-decided spots as they approach and disappear over the horizon. The imaging modes introduce more pointing error, and thus overlap error, in the system because of differences in the predicted positions of the satellites, as communicated in the last command cycle and their actual positions. The predicted positions and associated commands for who will be the reference satellite dictates how each satellite will slew to point at which ground spot.
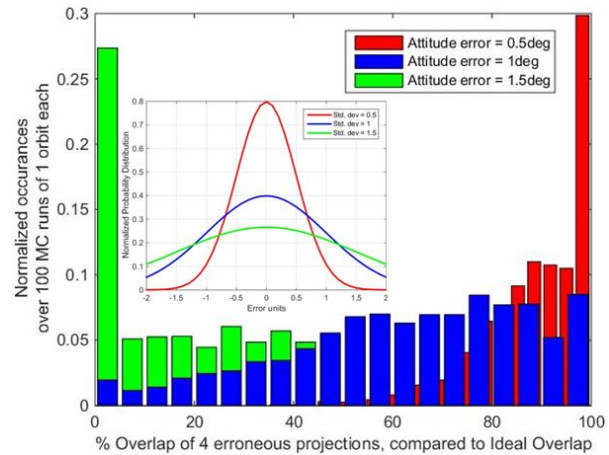

Figure 10: Normalized histograms of percentage overlap of the worst B/L cluster produced from 100 Monte Carlo (MC) runs as a function of varying attitude error input (inset), represented as a Gaussian with zero mean and varying standard deviation (per color).

A nominal relative position error of ±2 km causes a ±0.07° error in pointing ((5), which creeps up to ±0.5° for a ±15 km error. Current GPS systems easily provide within 2 km error[46]. Current propagation software such as STK's HPOP demonstrates that when satellites, that were initially

9

separated up to 10° in true anomaly, are propagated over a year, the time period between predictions and actual values are off by up to 3 seconds within a matter of 7 days. Eccentricity induced in a perfectly circular orbit, as will be explained later, is the cause of these time period mismatches. RAAN differentials between satellites do not show this large a time period change. A 3 second time error roughly corresponds to a 15 km distance error, which accumulates in a week. Propagation error (15 km) added to determination error (2 km) adds up over a week and leads to >0.5° pointing error over and above what the ADCS systems can achieve (best case, 0.5°) for imaging mode operations. Therefore, to keep pointing errors <1° and ground spot overlaps >70%, commands for the reference satellite sequence, waypoint sequence and satellites states should be sent to the cluster every 3-4 days. To reduce the frequency of commands, better autonomous processing and intersat communication, or better position control and orbit prediction capability is needed.

Slewing Maneuvers for Co-Pointing—To evaluate slewing abilities of the baseline clusters, the instrument sensor for all the satellites is assumed to be located on the –X face of the local body frame. When a satellite is at the origin of the LVLH frame and pointing at nadir, the X-axis of the satellite and the X-axis of the LVLH frame (radial, pointing downward) are perfectly aligned. This position along with the corresponding Y and Z axes aligned is the normal quaternion for any of the satellites i.e. $[0\ 0\ 0\ 1]^T$. It is also nominal imaging mode for a satellite at the LVLH origin. Non-reference satellites have to tilt their line of sight (LOS) and therefore reorient from the normal quaternion in order to point their sensors on the X-face to the ground below the reference satellite. If the satellite is located at an azimuth φ on the X=0 plane from the Y-axis and subtends an bore sight viewing angle ψ at the LVLH nadir, then the new quaternion, as expressed in (4) with respect to the normal quaternion, is given by $\hat{n}$ in (11). The algorithm is essentially [0 1 0] rotated about the X-axis by (φ – 90°), and then ψ about $\hat{n}$. Additional calculations will be needed if the roll about the payload pointing direction needs to be controlled, such as in the case of a rectangular FPA.

$$\hat{n} = \begin{bmatrix} 1 & 0 & 0 \\ 0 & \cos(\Phi - 90) & -\sin(\Phi - 90) \\ 0 & \sin(\Phi - 90) & \cos(\Phi - 90) \end{bmatrix}\begin{bmatrix} 0 \\ 1 \\ 0 \end{bmatrix}$$

$$\hat{n} = \begin{bmatrix} 0 \\ \sin(\Phi) \\ -\cos(\Phi) \end{bmatrix}$$

(11)

The instantaneous quaternion for any satellite at an azimuth of φ (from +Y or along-track direction) and at a bore sight angle of ψ from the LVLH nadir at any point of time in the cluster orbit is given in (12). This quaternion represents rotation from the body frame to the LVLH frame. An additional set of standard quaternions[33] are applied to rotate the LVLH frame such that its X-axis (HCW-X) is continuously pointed to the Earth Center.

$$q = \begin{bmatrix} q \\ q_4 \end{bmatrix} = \begin{bmatrix} \hat{n}\sin\left(\dfrac{\psi}{2}\right) \\ \cos\left(\dfrac{\psi}{2}\right) \end{bmatrix}$$

$$= \begin{bmatrix} 0 & \sin(\Phi)\sin\left(\dfrac{\psi}{2}\right) & -\cos(\Phi)\sin\left(\dfrac{\psi}{2}\right) & \cos\left(\dfrac{\psi}{2}\right) \end{bmatrix}^T$$

(12)

The quaternion associated with the body X axis of the satellite is zero without any loss of generality because the X-axis corresponds to the line of sight of the satellite sensor. The orientation about that axis is not of interest with respect to payload pointing. In the future as I design the solar panel or radiator orientation for the power or thermal systems respectively, q_1 will also be of interest and may need to be controlled. The required body angular rate, ω, can be found by differentiating the required quaternions in time (numerical first difference methods employed) and using (13) to solve for ω. The quaternion components are defined in (4).

$$\dot{q} = \frac{1}{2}\begin{bmatrix} \text{skew(q)} + q_4\text{I} \\ -q^T \end{bmatrix}\omega = Q(q)\omega$$

$$\text{Where}\quad \text{skew(q)} = \begin{bmatrix} 0 & -q_3 & -q_2 \\ q_3 & 0 & -q_1 \\ -q_2 & q_1 & 0 \end{bmatrix}$$

(13)

The body angular rate and accelerations required for 4 satellites in any of the baseline configurations can be calculated using first differences followed by the method above. The results for one orbit for a baseline cluster configurations (both best and worst from Table 2) are shown in Figure 11. The cluster has four satellites with 3 different RAANs, maximum 5 deg separation. Since they have only differential RAAN and TA, maximum variation is especially seen in the cross-track direction (triangular markers). While Figure 11 plots the variation over one orbit, the best 65% of the horizontal axes can be selected (by setting initial conditions appropriately) for science operations because BRDF imaging is expected to occur only during orbit day.

The reference satellite (black) and satellite with a TA offset (green) do not need any ADCS control in the LVLH frame (ignoring disturbing torques) because they point at the same LVLH spot at all times. Therefore, they are just a dot in Figure 6 and a flat line at zero in Figure 11. However, a continuous slew 0.06° per orbit is required for the reference (black) satellite, so that it continuously points at the Earth as it flies around the orbit. Similarly, all other satellites need additional slew (a maximum of 0.06°/s) to remain Earth-pointed. Since the angular slew requirements for Earth pointing are 2 orders of magnitude greater than the angular requirements of co-pointing in the LVLH frame, the former has not been added in Figure 11. The top plot, instead, demonstrates the accuracy to which we need to control the LVLH slew and how it is dependent on cluster architecture. If yaw-pitch slew were to be added to the top plot, the body pitch (dotted) lines will show a bias equal to the angular rate (mean motion = 0.06°/s) of the orbit for the black curves

and equal to part of the bias for the other curves. Negligible change is seen in the right plot, even with yaw-pitch control added, because the Earth pointing slew is a smooth one at constant angular rate.
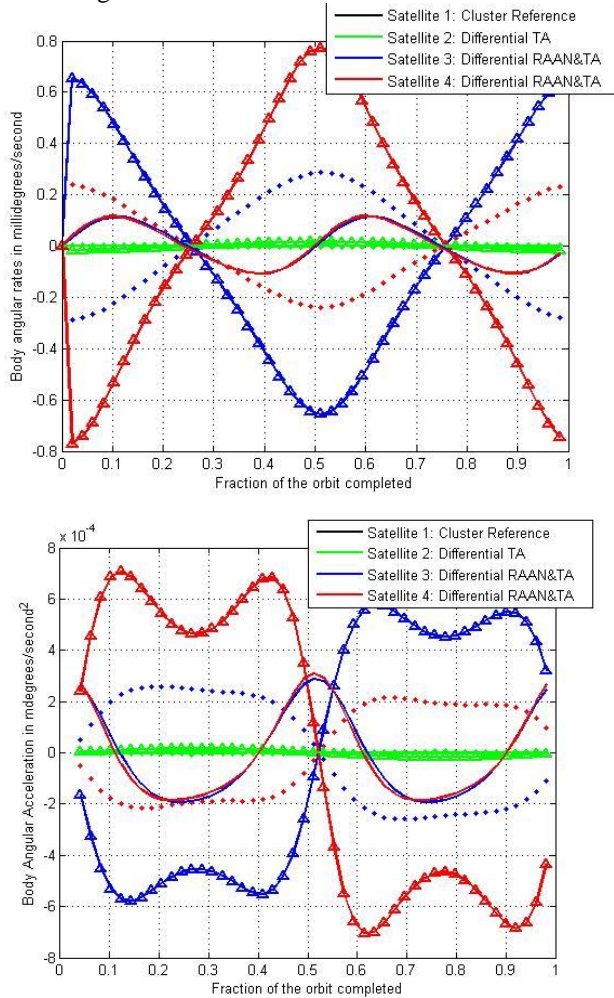

Figure 11: Body angular rates (top) and angular accelerations (bottom) in the LVLH frame required for each satellite in the best B/L configuration to point its payload consistently at the reference satellite's nadir point. The satellites are marked in different colors and ω_x (body pitch - dotted), ω_y (body roll - triangular markers), ω_z (body yaw - regular) in line types.

Assuming a 6U CubeSat with standard specs, commercially available reaction wheels are capable of supporting the required slew rate for all the satellites. For example, MAI-400 manufactured by Maryland Aerospace Inc. has a momentum storage capacity of 11.8 mNms and a torque authority of 0.625 mNm[21]. Multiplying the maximum angular acceleration in Figure 11 with a 6U moment of inertia (MoI = 0.4 kg-m²) gives a maximum required torque authority of 2e-4 mNm along any axis. Payload pointing requires <0.03% of the reaction wheel torque and a significant amount is available for cancelling disturbing torques. Similarly, the maximum required momentum storage capacity can be calculated from the required body

rate differences, summing them and multiplying by 6U MoI. For the rates found in Figure 11 added to the Earth-pointing rate, the maximum momentum storage needed, at any time instant, is 0.8 mNms. Assuming cyclic momentum, as is apparent from the figure, continuous payload operations are possible using MAI-400 without any momentum dumping.

Previous analysis shows that 6U reaction wheels have plenty of authority to compensate[47], even if orbital disturbances are accounted for on standardized bus, including external (atmospheric drag, magnetic torque, solar radiation pressure and gravity gradient) and internal (reaction wheel imbalance, propellant slosh, solar panel flex mode) disturbances. Reference[47]'s authors claim that the momentum accumulated over one orbit using torques from the worst possible case in the ARAPAIMA mission can be dumped with their three-axis thrusters with a single orbital maneuvering thruster. Simulations for my baseline scenario (650 km, 51.6 deg) and a residual magnetic moment (RMM) of 0.1 Am², agree with the torque values, however the momentum exceeds MAI-400's storage capacity. Instead, when an RMM of 0.01 Am² is used, in keeping with simulations and referred tests in [48], 2.8 mNms of momentum is found to accumulate per orbit. Assuming all of it to be secular and required to be dumped, MAI-400 needs to be de-saturated every 6 hours. For MOI = 0.4 kg-m² and a 20 cm moment arm between two thrusters per degree of freedom (12 DOF in all), each desaturation maneuver will need a ΔV of 0.0295 m/s. The annual budget then translates to 43 m/s for each wheel, which is a lot for cold gas thrusters but can be handled with electrospray propulsion because of the low thrust requirement. Dumping 11.8 mNms translates to an impulse requirement of 0.118 N-s, which can be fulfilled by thrusting 200 µN thrusters for 10 minutes during the eclipse, non-science operations phase. Alternatively, magnetic torquers can be used for desaturation as will be done in the MicroMAS mission whose momentum storage requirements are an order of magnitude greater than the currently presented mission[33].

While all the slew analysis above is performed for Imaging Mode#1, it is applicable to Mode#2 with an additional slew to change the reference satellite every ~10 minutes. Similarly, Mode #3 is also feasible because a similar amount of slew is required every ~10 minutes, as each satellite switches from tracking one waypoint to another. MAI-400's torque authority allows enough slew to reorient the payload from pointing at the ground spot below one leader satellite to another. Since the temporal resolution of my simulations is one minute, a reorientation within that time span shows no effect on performance. Assuming a maximum of ±60⁰ slew to change reference satellites (Mode #2) or waypoints (Mode #3), a 2 deg/s of slewing is needed. Such a slew will accumulate 13.9 mNms of stored momentum and need a torque of 0.465 mN. Since the former exceeds MAI-400's capacity, higher capacity reaction wheels will be needed for the imaging mode slew maneuvers. Blue Canyon's Model #RWp100 at 300 g, <2 W, 4 mNm of torque and 100 mNms of capacity is an ideal candidate.

Propulsion
The propulsion module calculates the ΔV to initialize and maintain formations and constellations, and evaluates COTS capabilities to support the same[21]. The process and feasibility of some baseline designs are shown below. The propulsion subsystem is found to be dependent on all architecture variables – altitude, inclination, RAAN-TA combination and number of satellites – in terms of initialization of the cluster and maintenance against differential J2 and drag.

*Initialization—*Constellations or formations can be initialized, both in terms of differential RAAN and TA, either using separate hosted payload launches[23], propulsion from the carrier launch vehicle (LV) such as Orbital Sciences Corporation's Pegasus rocket[5], propulsive from a propulsive adapter such as Spaceflight Inc's SHEPRA[49] or the spacecraft's internal propulsion (cold gas or electric). LV propulsion is difficult to negotiate unless the constellation is the primary payload. The SHERPA can be used as the propulsion provider in case a secondary launch is selected and one does not want to use spacecraft fuel. It is very difficult to initialize constellations with multiple RAAN planes because of the plane changes involved, which are very expensive. A possible strategy to reduce resource expense is to deploy planar groups of satellites followed by satellite deployment within the same plane.
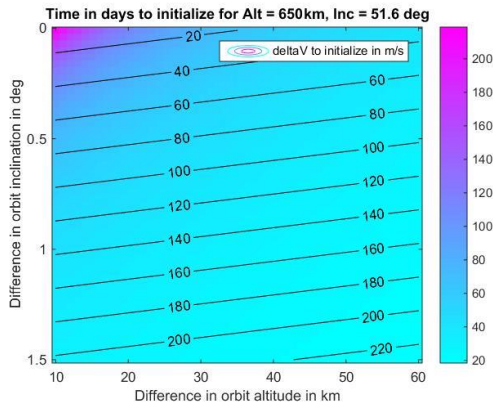

Figure 12: Time-ΔV trade-off for moving 2 satellites from zero to 5° apart in RAAN as a function of differential altitude and inclination, using chemical propulsion. The colors are time in days and the contours are ΔV in m/s.

To minimize the requirements imposed on LVs for achieving a large RAAN spread, a possible strategy is to launch the satellites into a differentially different altitude and inclination than the chief orbit, wait for precession to correct it to the target RAANs and, if required, use onboard propulsion to correct the differentials. The differential deployments can be done using LV fuel, a propulsive adapter or spacecraft fuel. Trades include the science time lost as opportunity cost, ΔV for the LV to initialize and ΔV

for the satellites to correct themselves. For example, Figure 12-top shows the time and ΔV required to move two satellites apart by 5° when they are launched into 650km+Δa and 51.6°+Δi. The separation is inspired from the baseline formations in Table 2. Very clearly, time required increases and fuel required decreases (by different amounts) with decreasing Δa and Δi. It has also been found that time increases by increasing chief altitude and inclination, far more due to the latter. It remains a design engineer's choice whether she would like to spend 20 days and 220 m/s or 140 days and 20 m/s to initialize the 2-sat formation. Quite obviously, the resource requirements to initialize a uniform constellation are much more because the RAAN separations are up to 90°, corresponding to a few years of precession to stay within 50 m/s of fuel. A brute force of 90° plane change would take ~10 km/s compared to the 55 m/s with 600 days.
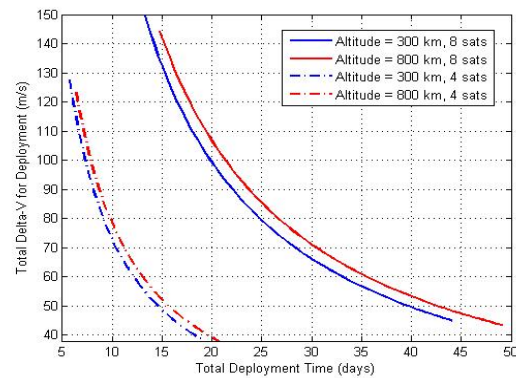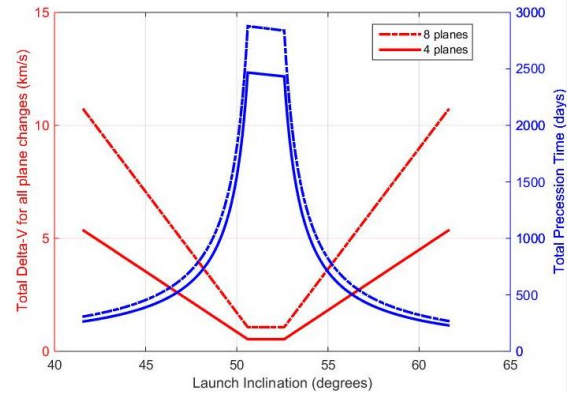

Figure 13: Trade-off between total ΔV and deployment time required to deploy [Top] a carrier into 4 or 8 equally spaced planes, as a function of initial launch inclination, where the ISS orbit (400 km, 51.6°) used as reference; [Bottom] 4 or 8 equally spaced satellites in the same plane, Time is a function of the phasing orbit.

Another possible strategy for planar separation is to launch into a plane with a slightly different inclination than the desired, wait for J2 to precess each plane to each required RAAN and perform a ΔV to change the inclination when they do. This method uses less than half as much fuel as a brute-force plane change would for deploying at all RAANs, and can be optimized further by separating groups of satellites into different launches. Greater the difference between the injection and desired inclinations, faster the

---

precession, however, more is the required fuel for changing the planes. Figure 13-top shows the planar deployment into 4 and 8 planes for the ISS orbit (400 km, 51.6°), where the planes are equally spaced as in a Walker constellation. If the ΔV comes from the launch vehicle, it will have to sequentially deploy each satellite group at each RAAN plane. It is obvious from the figure that for a 4-plane constellation, if one wants to be fully deployed within a year, an initial launch at ~45° or ~58° inclination is needed along with ~3.5 km/s of ΔV (<1 km/s per plane). The fuel expense is much more than the previous strategy because of the lack of differential inclination. All constellation architectures in the generation process have been capped off at a maximum of 8 planes to keep the expenditure for initialization realistic. The fuel requirements for achieving large RAAN spreads, strategy notwithstanding, can be traded against the cost to purchase multiple launches, the time in between them (including schedule slips for secondary launches) and performance loss or gain due to sequential launches being at different altitudes and inclinations. The mission designer may then make a choice to go with separate launches vs. LV or satellite-driven propulsion that comes with its own science opportunity and fuel cost.

Electric propulsion was found to be less suitable than chemical propulsion for the above RAAN changes, when spacecraft fuel is used in either case. This is attributed to the greater required ΔV (due to low-thrust maneuvers in (2) and, more importantly, the long duration associated with those maneuvers due to nanosats' power constraints ((3). Assuming a maximum power of 50 W at 60% efficiency, the available thrust is 0.0061 N. A 5° plane change will then take ΔV~1 km/s and 32.5 days. Figure 12 shows that the same plane change is possible in the same time for as low as 100 m/s. ΔV~1 km/s in electric propulsion with Isp = 1000s corresponds to 1.67 kg of fuel while ΔV~100 m/s in cold gas or chemical propulsion with Isp = 65 s or 150s corresponds to 2.5 kg or 1 kg of fuel respectively. Electric maneuvers prove to be less optimal even in terms of mass to orbit for plane changes, owing to the large ΔV needed.

A possible strategy for satellite deployment in the same plane to achieve TA spread, is to use atmospheric drag manoeuvres as proposed by the CYGNSS mission[50], or use ΔV burns to enter and exit an appropriate phasing orbit to spread out the TA of the satellites. CYGNSS proposes to launch its single plane, 8 satellite constellation within 200-350 days by deploying its solar panels strategically to manipulate drag. In the propulsive approach (using spacecraft fuel), a range of 30 to 200 phasing orbits have been analyzed. The greater the size of the orbit, the faster is the TA deployment because of faster differential phase change between the satellites being separated. However, more ΔV is needed to achieve larger phasing orbits via Hohmann transfer. Figure 13-bottom shows the deployment of 4 or 8 satellites, equally spaced in the same plane for two extreme LEO altitudes. The altitude dependence is insignificant compared to the time or ΔV required for the

size of phasing orbits. While the required ΔV is lesser than for planar deployment, LV fuel cannot be used for this purpose. The satellites themselves have to carry the required capability. For a 4-sat constellation, each satellite must have 10 m/s available to deploy within 20 days. Commercial cold gas propulsion systems can support such requirements. For example, AustinSat's 1U system[6] (scalable linearly up to 3U), supports 6DOF thrusters with ΔV of 40 m/s, minimum impulse bit of 0.125 mNs and flight heritage on STS-116 MEPSI. If mission fuel is a sparse resource due to orbit maintenance needs, the CYGNSS approach may be used.

Initialization of a formation is less expensive or difficult than constellations, because the differential Keplerian elements are lesser in magnitude. With the availability of several imaging modes and ADCS to support them, a degree of error in initialization can be compensated for during operations. Satellite deployment in the same plane for a formation is also cheaper because the maximum TA differential is 5°. Deploying 4 satellites takes an absolute maximum of 26 days and 3 m/s or 7 days and 9 m/s in total, trade-offs applicable as before.

Maintenance—Since all the baseline formation configurations have only differing RAAN and TA, the only major disturbance forcing the clusters apart is differential drag and unpredictable J2 due to the spherical harmonics of Earth's gravity. The satellites may experience different atmospheric densities at different times. Our baseline study at 650 km needs ΔV<10m/s in a year for altitude maintenance and, in fact, angular coverage is acceptably maintained over a year even with no corrections as will be demonstrated below. The view zenith angles (VZA) subtended at the ground target shows little variation over the period of a year due to the above differential drag or J2, for the baseline cluster in Table 2. VZA can be calculated from Figure 5 and eq (9), when the satellites are separated along-track due to differential TA, or cross-track due to differential RAAN (maximum at equator) or inclination (maximum at highest latitude covered). The change in maximum VZA per orbit is less than 1° when differential RAAN or TA is 3° (Figure 14-row 2) or 5^0 (Figure 14-row 1). Science impact analysis in [51] has shown that <5° of VZA difference does not affect BRDF estimation errors significantly. VZAs obtained from differential RAAN deteriorated less than those from differential TA because the drag effects and J2 effects countered each other. All the VZAs are measured at the Equator because they are zero at the poles for diff. RAAN.

When differential inclination, instead of RAAN, is used to obtain the cross-track VZA, the deterioration in angular spread without propulsive corrections is significantly more (Figure 14-row 3,4). Further, more differential inclination than RAAN is required to obtain the same maximum cross-track VZA. 0.2° (2°) of differential inclination can attain only 5° (20°) measurement angle initially at the highest

---

[6] http://austinsat.net/cold-gas-thruster-for-cubesats/

latitudes as seen in Figure 14-row 1(2) and these angles collapse to zero in less than a month due to differential J2 effects. J2 due to different inclinations causes the satellite's orbits to rotate and increase differential RAAN. This increases the cross-track VZA at the Equator linearly, and after a point, the satellites lose sight of each other causing the saturation in the curve. J2 also changes the eccentricity and argument of perigee, however this is insignificant for circular orbits. The next section discusses the J2 effects on all Keplerian elements when eccentricity is induced in circular orbits, propagated over time.
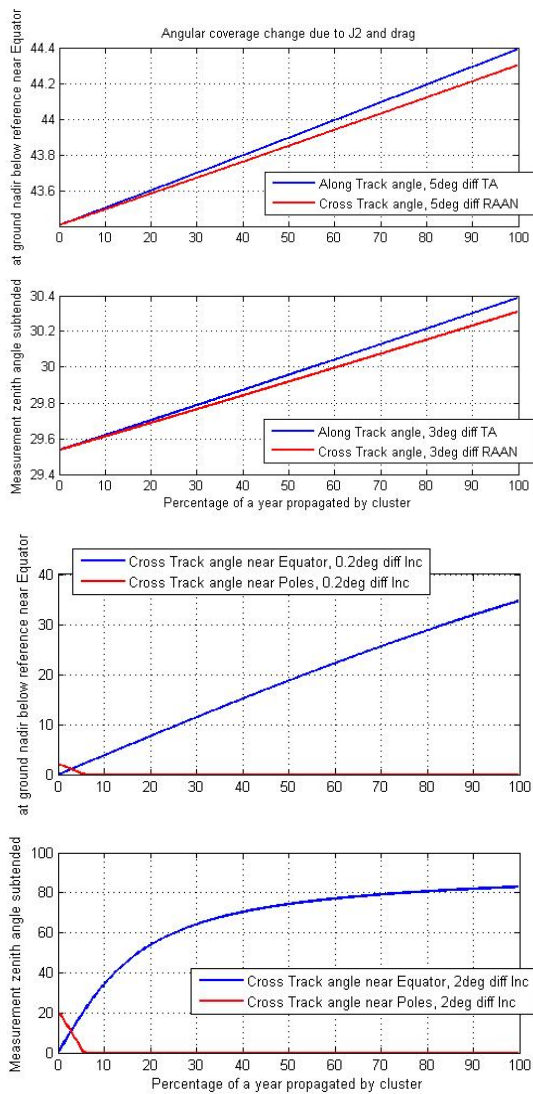

Figure 14: VZA at the reference satellite's nadir as subtended by a non-reference satellite with differential RAAN [row 1,2] and inclination [row 3,4]. Angular coverage is more for more differential TA or RAAN, same for TA and RAAN (blue and red respectively). The rate of change remains the same. Angular coverage is more for more differential inclination (row 3,4) but cannot be sustained at the poles (red) and, without maintenance, angular coverage at the Equator (blue) increases till the sats no longer see each other.

Although differential inclination is the only way to attain cross-track angles at the poles, J2 effects do not allow these angles to be sustained without propulsion. Not only is the angular spread pushed to the Equator, this spread is not stable either. Maintenance of such a cluster is very expensive because 650 km orbits with inclination differences of 0.2° and 2° cause RAANs to increase daily by 0.0098° and 0.0991° respectively and ΔV required to correct these rotations is 0.584 m/s and 5.909 m/s respectively. Differential inclination and large differential eccentricity are impossible to maintain using current cubesat technology.

Propagating different orbits with varying differential RAAN and TA using the High Precision Propagator (HPOP) on STK showed that, over a year, differential RAAN does not break the formation but differential TA does because of higher harmonic effects that are unpredictable using simple gravity models. Higher order spherical harmonics of gravity are needed to better predict these uncertainties, and even then the real environment is expected to present new surprises. The satellites drift in differential TA is because globally-varying gravity changes eccentricity of the orbit of each satellite by different amounts. Gravity harmonics rotate the argument of perigee as a function of eccentricity, thus the perigee of each satellite's orbit is caused to rotate differently. This translates to an irregular phase difference in the orbits' time period and thus changes the differential TA.

To analyze the TA drift over time as a function of initial conditions or propagator used and its impact on maintenance resources, a few satellites, inserted differently and propagated differently were simulated. At a 650 km, 51.6° orbit (base lined), a satellite is expected to move 5° in 81.2 seconds. If a satellite (say, Sat 2) is inserted lagging a reference satellite (say, Sat 1) by 5° and if a satellite (say, Sat 3) is inserted 81.2 seconds after a reference satellite, then all three satellites should behave similarly if gravity was uniform. However, in reality, they behave very differently. Not only do Sat 1 and Sat 2 diverge due to going over different regions of the Earth at different times (as pointed out before), Sat 2 and Sat 3 diverge with respect to Sat 1 in *different* ways. Since Sat 3 is inserted 81.2 seconds later in the earth rotating frame, it is inserted at a different point on the earth fixed frame and therefore experiences slightly different gravity harmonics compared to Sat 1. These slight differences cause different relative trajectories, when propagated over a year, irrespective of the propagator used. In fact, the relative trajectories are different for different propagators and initial conditions as well. Figure 15 compares the mean anomaly between Sat 2 and Sat 1 (blue) and Sat 3 and Sat 1 (red), using AGI STK's High Precision Orbital Propagator (HPOP) and using NASA Ames' in-house orbital propagator[52]. Mean anomaly has been calculated as the angle subtended at the centre of the Earth by the two satellites. Simply subtracting the mean anomaly of the satellites results in erroneous results, because STK calculates mean anomalies from the satellite's position and velocity vectors. The HPOP causes these

vectors to vary a lot instantaneously, depending on the satellite's position over the fixed Earth.
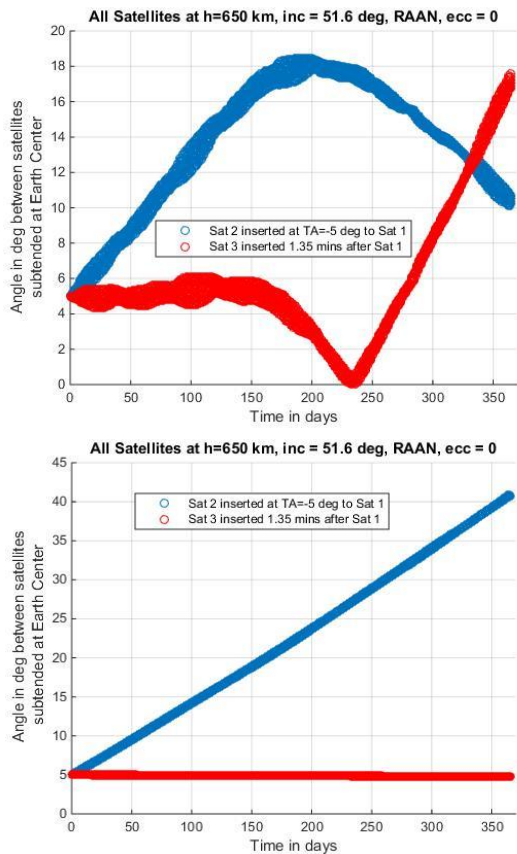

Figure 15: Earth centric angle (analogous to TA) between 2 satellites inserted differentially, in space (blue) and in time (red), on the same orbit with respect to a reference satellite at 650 km, 51.6⁰, RAAN/TA/e = 0. The orbits were propagated using NASA ARC's LightForce propagator (top) and using AGI STK's HPOP or Astrogator propagator (bottom).

The HPOP predicts no change in the differential TA between reference satellite and one inserted 81.2 seconds after it (Sat 3); but predicts that the differential TA will increase from 5^0 to 40^0 in a year if the satellite is inserted trailing the reference satellite (Sat 2). The Ames propagator predicts that very little change in the differential TA between Sat 1 and 3 will be seen for the first 5 months, followed by a decrease the differential as Sat 3 approaches Sat 1, followed by a linear increase as Sat 1 continues to fall behind. For Sat 2 with respect to 1, it predicts the same rate of increase in differential TA as HPOP predicted. However, 6 months into the mission, the differential TA stops increasing and starts decreasing instead. I attribute the difference in behaviour to different ways of modelling spacecraft propagation over the WG84 model of the Earth as well as the cumulative effect of being introduced at different locations on the earth, even if initially very small. When the satellites in the STK HPOP simulation are introduced as Brouwer-Lyddane mean, short elements instead of osculating, Keplerian elements, the same initial conditions

result in different relative behavior. Figure 16 shows the differential anomaly between Sat 2 (blue) with respect to the baseline satellite, when both were inserted within 5° of each other in the same orbital plane as before, but this time as mean elements. Unlike Figure 15, Sat 2 does not fall back from trailing Sat 1 from 5° to 40°. Instead, it catches up with Sat 1, resulting in a virtual collision after a year. If it is inserted 5° leading Sat 1 (and called Sat 4 in Figure 16), it falls back linearly, virtually collides with Sat 1 after 8 months and then increasingly trails Sat 1.
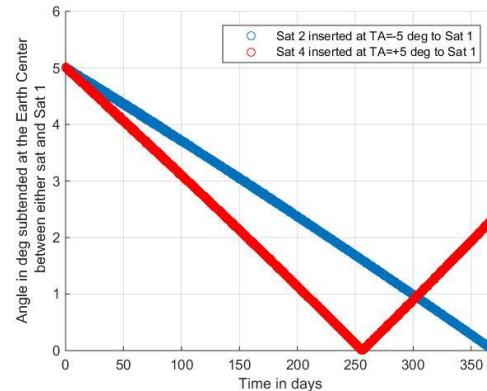

Figure 16: View Zenith Angle (VZA) subtended by one satellite on the ground below another satellite when the 2 satellites inserted differentially in Brouwer-Lyddane mean, short, true anomaly of 5^0 trailing (blue) and 5^0 leading (red) a reference satellite, as in Figure 15. The orbits were propagated using AGI STK's HPOP or Astrogator propagator.

Propulsive manoeuvres will be needed to correct for drifting relative TA for two reasons. First, too much diverging drift – for example, assuming the HPOP scenario in blue from Figure 15 - will break the formation. Second, too much converging drift – for example, assuming the HPOP scenario in red from Figure 16 or the Ames propagator scenario in red from Figure 15 – will cause the risk of inter-satellite collisions. The amount of maneuvers is also unpredictable because the TA drift depends on how the satellites in the cluster are inserted and different propagators have predicted different behaviour for the same initial conditions. Assuming the worst case scenario assuming HPOP to be true (Sat 2 in Figure 15), 35^0 of TA drift needs to be corrected in one year. For the worst case scenario assuming the Ames propagation to be true (Sat 2 – Ames propagated in Figure 15), 14° of TA drift needs to be corrected. TA corrections are possible using a phasing orbit, similar to the differential TA initialization. There is a trade-off between required ΔV and time, depending on the size of the phasing orbit as seen in Figure 17.

While Figure 17 shows the cumulative resources required for annual corrections, in reality, maintenance against random disturbances will need to be performed monthly, especially to mitigate collision risks. Assuming the availability of 1-5 days per month for these corrections, the fuel needed per satellite is as low as 0.4-1.8 m/s. In the

worst case scenario where maintenance is restricted to only 1 day per year, <35 m/s of cold gas fuel is needed (Figure 17-red) which is available in a <1U box provided by AustinSat.
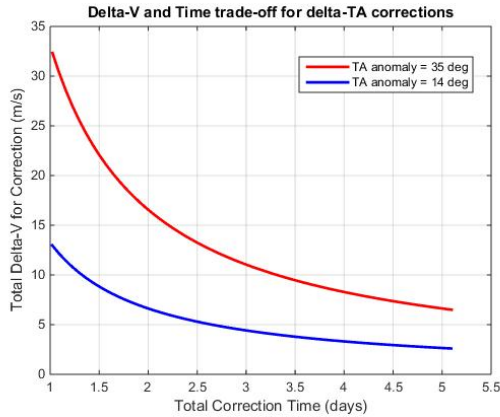

Figure 17: Correction fuel vs. time required for reducing the divergent true anomaly (calculated equal to earth centric angle in Figure 15) between any pair of satellites in the same orbit at 650 km, 51.6^0. The trade-off is achieved by varying the size of the phasing orbit.

Table 3: Propulsion budget per satellite in the CubeSat baseline formation cluster in Table 2. The leader sat takes no time or fuel to initialize.

ΔV	Time	Comments
Initialization		
10 to 220 m/s	200 to 20 days	Trade-off between fuel-time for 2 sats separated in RAAN
1 to 3 m/s	26 to 7 days	Trade-off between fuel-time for 3 sats separated in TA
Maintenance against atmospheric drag (per month)		
0 to 4 m/s	~1 hour	From 500 km to 400 km (electric feasible)
Maintenance against unpredictable J2 (per month)		
0.4 to 1.8 m/s	1 to 5 days	To correct induced eccentricity (electric feasible)
Reaction wheel desaturation (per month)		
<11 m/s	10 minutes	Total for all 3 wheels (electric feasible)

Since there is no predictability in determining the behaviour of differential TA over a long time span, cluster missions should incorporate flexibility and accept that stringent relative positioning will come at high costs. Long-term position uncertainty in the absence of any maintenance highlights the importance of multiple imaging modes to compensate. Using satellite position information, as known a few days in advance, to decide the ordering of reference satellites and then slewing to implement it (Mode #2) introduces a much-needed system flexibility. One year into the mission without any maintenance, when every satellite may not see the others, waypoints can be decided a couple of orbits in advance and all satellites commanded to look at

them when they pass within its view (Mode #3). Waypoints can be selected based on the expected position of the satellites that provides an expected angular spread within an acceptable time period. As before, ground control can optimize the angular spread and select waypoints with least expected albedo or BRDF RMS error, depending on the biomes the cluster is expected to go over.The propulsion budget, for initialization and maintenance for the baseline (best) configuration in Table 2 can be summarized in Table 3. Detailed analysis on required thrust profiles and de-orbiting budgets will be discussed in a future publication.

Communication

A cluster of nanosatellites collecting hyperspectral or even multi-spectral reflectance measurements with reasonable radiometric precision will generate more data than most current nanosatellite missions. Using the payload baseline design from [17], data generated by Acousto Optic Tunable Filters (AOTF) and Waveguide (WG) spectrometers are compared and current communication methods to downlink data assessed.

Since WG spectrometers are hyperspectral instruments, images at 12-bit resolution are collected for 86 wavebands imaged on its 1000×1000 FPA only during orbit-day ~65% of the orbit A radiometric resolution of 12 bits per pixel is considered sufficient, as indicated by the OSSE model[51] and validated against current, state-of-art BRDF instruments[7], [10]. If an image is generated every 1 km, or every two ground pixels, it translates to ~300 GBits of lossless, uncompressed data by one satellite in one orbit. This needs to be downloaded to relieve data and flash memory management needs on the nanosatellite. This orbital data may can be further compressed depending on the science requirements, but increased by using error correcting codes (ECC), depending on the error requirements. Assuming a 6:1 compression ratio (from SpaceCube, next section) and 1:2 increase due to ECC, about ~100 Gbits of data is needs to be down linked during every orbit. While the total amount of data down linked to Earth depends on the achievable data rate (link budget), number of ground stations available per pass, and the duration of each pass, 100 Gbits is too much for any combination of state-of-art. If an image is generated every 10 km, or the baseline swath of the reference satellite at lowest altitude [17], 10 Gbits of data is generated per orbit.

Since AOTF spectrometers are multi-spectral instruments that will image one band at a time, 14 bands are imaged every 500 m (largest pixel size at baseline orbit) at 12-bit resolution for 65% of the orbit. In keeping with [17], an image is generated every 7 km (baseline swath of the reference satellite at lowest altitude [17]) where each image has 70×70 spatial pixels and 14 bands, constrained by imaging time and not FPA size. This translates to 3 Gbits of data per orbit which is less than a third generated by WG spectrometers. The spacecraft must have enough on-board memory to store one or more orbits of data (for example, 128 GB flash SD cards) in case downlinks are not possible

or to support validation of received data on the ground before discarding it on orbit.

Available Ground Stations and Frequency Bands—An average ground station allows a conservative 3 minute window for downlink with elevation restrictions to >25°[36], and more than 10 minutes with elevation restrictions to >10^0[34]. These downlinks are also often duty-cycled or interspersed with commands and acknowledgments, with additional time required for link acquisition. Therefore, a conservative downlink time requirement of 3 minutes per orbit is assumed. I estimate that approximately a 55 Mbps downlink rate is needed to downlink 10 Gbits of data in 3 minutes using one ground station per orbit. For the AOTF design, a 16 Mbps link is required. As a simplifying assumption, the data rate does not assume margins for headers and satellite health packets because it is small compared to the bulk of science data.

Current nanosatellite state of the art links are on the order of 1 Mbps[21]. This suggests that either a large number of ground stations are needed, or that advanced technologies using higher rate miniaturized radios (X band or higher) or nanosatellite optical communications are necessary. X-band, Ka band and laser-comm solutions achieve their higher rates using a narrower, higher-gain beam, which need additional pointing capability and orbit determination capability. The mission is already expected to have high pointing capabilities due to the co-pointing requirement enforced by science (ADCS section), therefore aside of beam defocussing, no additional capability is required to enable very directional communication. X or Ka band downlinks from cubesats in the literature review are appropriate.

The above frequency requirements have been assessed assuming the availability of a 3 minute, 55 Mbps (WG) or 16 Mbps (AOTF) downlink in every orbit. In reality, such an assumption may not be feasible because of the uneven distribution of ground station networks. I used AGI STK's HPOP propagator to simulate a baseline satellite at 650 km, 51.6 deg at one minute time steps and calculated its access (at or above 25^0 elevation) to ground stations placed at the locations of the Deep Space Network (DSN) - Goldstone Deep Space Communications Complex (35°25′36″N, 116°53′24″W) outside Barstow, California; Madrid Deep Space Communication Complex (40°25′53″N 4°14′53″W), west of Madrid in Spain; Canberra Deep Space Communication Complex (CDSCC) in the Australian Capital Territory (35°24′05″S 148°58′54″E). The ground stations and the corresponding access times show that the satellite has 59 one-minute accesses with either of the stations at varying range distances or slant heights as seen in Figure 18. Since a 650 km high satellite completes 15 orbits per day, the STK analysis confirms the availability of 3 minutes available per orbit, even if the data is not down linked every orbit. Currently available 128 GB flash cards suggest that more than 100 orbits of data can be stored on-board until the next downlink becomes available.
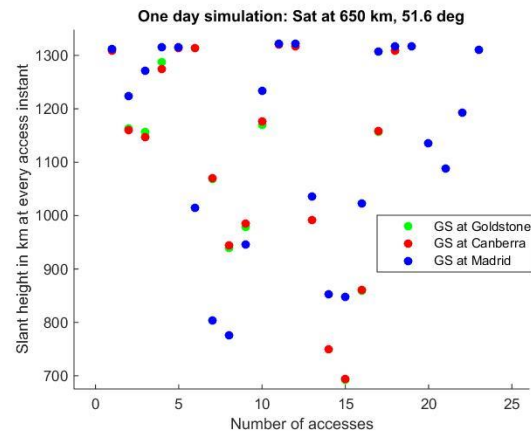

Figure 18: Scatter plot of the 59 times a satellite accessed any one of the DSN ground stations over the period of 24 hours, at an elevation more than 25^0, and the corresponding range as simulated on AGI STK.

While the DSN is not optimal for LEO constellations due to frequency limitations and usage constraints, it has been used only as an example in this section. The real links will be performed using NASA's Near Earth Network[7] (NEN) where in NASA owns 6 ground stations and contractually uses 10 others. The NEN also provides tracking, telemetry and command services and supports the S and X bands.

Currently supported data bandwidths, CubeSat hardware and available ground stations make it obvious that data generated by AOTFs can be downlinked far more easily than data by WG spectrometers. AOTFs can either use X-band links with 3 NEN ground stations or S-band links with 6 or more NEN stations. ISS inclination orbits are faced with a significant disadvantage because they are covered by less than 50% of the NEN stations. WG spectrometers, on the other hand, need a laser communication link (50 Mbps max) or a futuristic Ka-band link with a couple of ground stations, or current S and X links with more than a dozen ground stations. Improving data rates not only depends on the improving bandwidth but developing faster A/D converters for the SDR radio boards that will sample data and providing the power to support the same. AOTFs are thus far more supportable in terms of communication than WG spectrometers. The next section describes using ISLs as another approach to downlink more data than data links and ground stations can support.

Viability of Inter-satellite Links—Providing a high capacity downlink on one leader satellite and having all the others transmit their data to it through inter satellite links (ISL) was considered as an architectural alternative. NASA ARC's EDSN program (expected launch in 2015) plans to demonstrate ISL and the using-one-captain strategy among 8 1.5U CubeSats [41]. ISL may be a big improvement in our mission, if technologically feasible using smaller antennas and inter-sat pointing knowledge and control, because of several reasons. *First*, it avoids atmospheric losses because

---

[7]http://esc.gsfc.nasa.gov/space-communications/NEN/nen.html

all links in our tradespace are at a height more than 500 km for a 650 km orbit. For any pair of satellites, the distance between them is calculated using eq. **(7**) and Figure 5. The maximum possible earth angle constraint is then calculated using a minimum ISL height (h$_g$) of 500 km in (8 below. All the satellites in a 650 km orbit are found to establish an ISL at >500 km as long as they subtend a maximum earth angle of 23° (true 100% of the time for all 36 pairs of potential RAAN-TA combinationd. *Second*, BRDF data at different angles has redundancy among themselves, so combining the images centrally before downlink will increase the compression ratio and decrease the total data needed to be down linked. *Third*, ISL consolidation of data avoids the need for every satellite to acquire and maintain a link with every ground station. 3X15 or 45 minutes of downlink for every satellite in the cluster, especially for large numbers, creates a high demand for ground station time and support, increasing costs. Sometimes access times between a ground station and two satellites may overlap, causing less available time for both. Competition for access can be reduced and the saved costs can justify ISL.

The proposed BRDF cluster needs large angular spreads, which results in very long ISL baselines. However, since direct downlinks are mostly over large slant distances, ISLs may not necessarily be at a big disadvantage. All overpasses by a 650 km satellite over 3 ground stations have been simulated in Figure 18, discussed before. The average range is 1127 km over all 59 minutes, which is even higher than the average range between the 800 km high satellite flying directly overhead.

In order to compare the data link distances between ISL and direct downlink, a cluster of 9 satellites was considered. The satellites were base lined to fly at a 650 km, 51.6° orbit with a differential RAAN and TA (in LVLH frame) corresponding to Reference [3]. All the architectures, per chief orbit, are generated are placing N satellites into one of these 9 slots, hence a study of ISL between these satellites

can be considered exhaustive. 36 pairs are possible among the 9 satellites, all of which trace a relative analemma[3] with respect to the other as seen in Figure 6. Figure 19 [Inset] shows the maximum and minimum ISL separations between each pair (per row) over one orbit. Maximum separations are expected to occur at the equator and minimum at the highest latitude of coverage.

While angular imaging is best done at the maximum distance or angles apart, communication is most efficient at the minimum distance apart. Data transfer between satellites should thus be performed at the highest latitudes when the satellites are eclipsed from the sun, so that it does not take any time from science operations. The square of the ratio of the slant distance to a ground station and the intersatellite distance can be used a metric for ISL data rates as compared to those achieved with direct downlink (link equation [34]). This simplifying assumption compares the two approaches only in terms of data rate, and ignores the atmospheric advantage and antenna size disadvantage of ISLs. Figure 19 – blue - shows the trade-off between maximum, achievable VZA between any pair of satellites and the number of times the pair's ISL (at minimum separation) exceeds a direct downlink rate. Figure 19 – red – plots the corresponding minimum ISL ranges. For example, if the intersatellite distance is 368 km, corresponding to a satellite pair separated in TA by 3° on a 650 km orbit, the ISL data-rate required would be 9.65 times more than transmitting to ground. However, the maximum VZA the satellites can achieve is only 30°. Since the blue vertical line represents equal data rates using ISL or downlink, satellite pairs to the right of the blue vertical line have faster ISL data rates than downlink rates. The ground slant distance is assumed to be the squared average of the distances in Figure 18-right. Cluster architectures containing only satellite pairs with ratio > 1 are likely to benefit from ISL. Architectures with mostly such pairs may also be identified and a strategy combining ISL and multiple downlinks used.
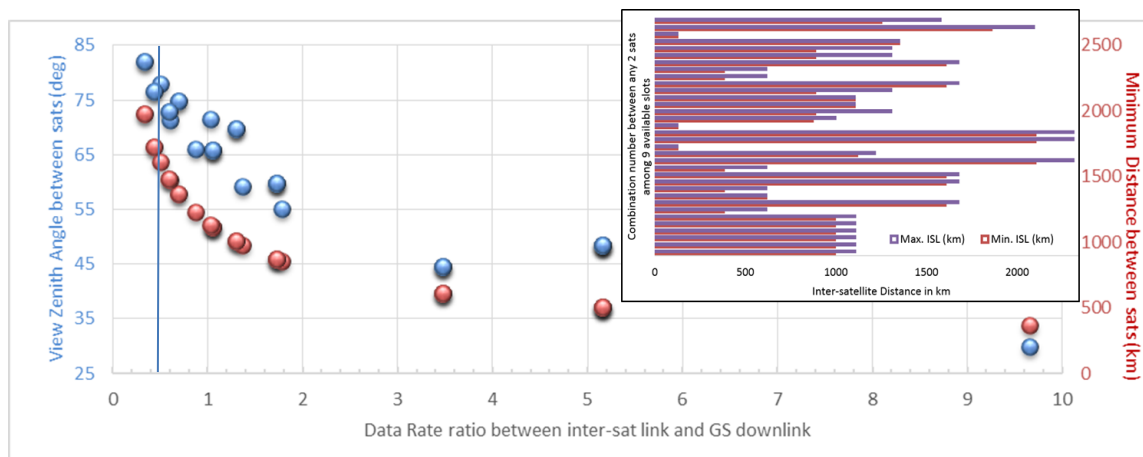

Figure 19: [Main] View Zenith angle (VZA) subtended between any pair of satellites vs. the expected decrease in required data rate if the two satellites were to transmit data via ISL instead of down linking to Earth. Satellite pairs to the right of the blue vertical line have faster ISL data rates than downlink rates. Right/red axis shows the minimum inter-sat distances between the corresponding pairs. [Inset] Minimum vs. maximum inter-sat distances between the satellite pairs.

On-board Processing

The on-board processing unit will take raw images from the payload module, process them for the communication downlink and also transfer them to GNC module as guidance information. One standardized COTS unit which fits the subsystem interdependencies and requirements is NASA GSFC's SpaceCube Mini - an on-board, modular processing unit. It has been described in the literature review and has shown a 6:1 reduction in downlink data by moving first stage ground operations on-board, to make cluster science data manageable.

The proposed processing module, shown in Figure 20, combines the capabilities of the GNC and processing module to aid both. The green sections indicate existing capabilities that will be leveraged and the red sections indicate development required during the build phase of this mission. Each individual section and the interface integrations have been tagged with logos to demonstrate the expected prime contributor, given that GSFC owns SpaceCube while MIT owns the DSM algorithms. The approach uses the position and attitude data estimated from the GNC module's GPS and star sensors to provide an initial guess for image co-registration. On-board image processing can not only compress the collected data and prepare it for downlink; they can also transmit the processed, sharpened image back to GNC. The GNC module can use this extra information for guidance, integrated with the estimator and controller modules (TRL 5) with heritage from the ExoplanetSat or MicroMAS studies[26]. The guidance algorithms thus leverage hyperspectral image processing algorithms from NASA Goddard Spaceflight Centre (GSFC) which can easily be coded into their SpaceCube platform.
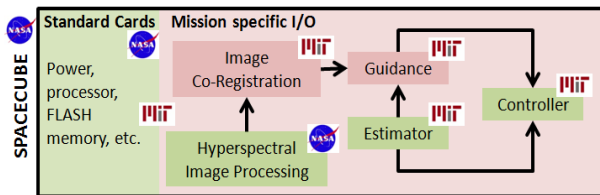

Figure 20: Proposed integrated onboard processing unit for cluster GNC and multi-spectral image processing. Green indicates existing capability and Red indicates that to be developed and/or integrated. Logos represent MIT or NASA-housed technology.

Future work includes testing these GNC algorithms on the high fidelity models of software, actuators, satellite dynamics and space environment that include natural disturbances, processing time, control bandwidths, actuator and sensor error propagations, latency, discretization, quantization and saturation. On-board data processing serves to reduce the amount of data for downlink and aids the communication module. The above GNC-processing integrated product can, if needed, be made generalizable to clusters with different mission goals and can allow for customization in terms of functionality, autonomy, number of spacecraft, satellite size, etc.

REFERENCES

[1] H. J. Kramer and A. P. Cracknell, "An overview of small satellites in remote sensing*," *Int. J. Remote Sens.*, 2008.

[2] M. Chopping, "Terrestrial applications of multiangle remote sensing," *Adv. Land Remote Sens.* 2008.

[3] S. Nag, J. LeMoigne, D. W. Miller, O. L. De Weck, "A Framework for Orbital Performance Evaluation in Distributed Space Missions for Earth Observation," in *IEEE Xplore, Aerospace Conference 2015*, Big Sky 2015.

[4] D. J. Diner, et al, "Multi-angle Imaging SpectroRadiometer (MISR) instrument description and experiment overview," *Geosci. Remote Sens. IEEE Trans. On*, 1998.

[5] X. Xiong, et al, "Terra and Aqua MODIS Design, Radiometry, and Geometry in Support of Land Remote Sensing," *Land Remote Sens. Glob. Environ. Change*, 2011.

[6] F. E. Nicodemus, *Geometrical considerations and nomenclature for reflectance*, vol. 160. National Bureau of Standards Washington, D. C, 1977.

[7] A. Lyapustin, et al, "Analysis of snow bidirectional reflectance from ARCTAS Spring-2008 Campaign," *Atmos Chem Phys*, vol. 10, no. 9, pp. 4359–4375, 2010.

[8] B. A. Wielicki et al, "Mission to planet Earth: Role of clouds and radiation in climate," *Bull. Am. Meteorol. Soc.*, 1995.

[9] T. Hilker, et al, "Inferring terrestrial photosynthetic light use efficiency of temperate ecosystems from space," *J. Geophys. Res. Biogeosciences*, vol. 116, no. G3, p. n/a–n/a, 2011.

[10] C. K. Gatebe, "Airborne spectral measurements of surface–atmosphere anisotropy for several surfaces and ecosystems over southern Africa," *J. Geophys. Res.*, 2003.

[11] P. Y. Deschamps, et al, "The POLDER mission: Instrument characteristics and scientific objectives," *Geosci. Remote Sens. IEEE Trans. On*, vol. 32, no. 3, pp. 598–615, 1994.

[12] B. A. Wielicki, et al, "Clouds and the Earth's Radiant Energy System (CERES): An earth observing system experiment," *Bull. Am. Meteorol. Soc.*, vol. 77, no. 5, pp. 853–868, 1996.

[13] C. Godsalve, "Bi-directional reflectance sampling by ATSR-2: a combined orbit and scan model," *Remote Sens.*, 1995.

[14] M. Abrams, "The Advanced Spaceborne Thermal Emission and Reflection Radiometer (ASTER)" *Int. J. Remote Sens.*, vol. 21, no. 5, pp. 847–859, 2000.

[15] A. Barducci, et al, "CHRIS-Proba performance evaluation: signal-to-noise ratio, instrument efficiency and data quality from acquisitions over San Rossore (Italy) test site," in *3-rd ESA CHRIS/Proba Workshop, Italy*, 2005.

[16] S. Nag, C. K. Gatebe, and O. L. De Weck, "Relative Trajectories for Multi-Angular Earth Observation using Science Performance Optimization," in *IEEE Xplore, Aerospace Conference 2014*, Big Sky, Montana, USA, 2014.

[17] S. Nag, et al, "Evaluation of Hyperspectral Snapshot Imagers onboard Nanosatellite Clusters for Multi-Angular Remote Sensing," in *AIAA Space Conference*, San Diego, 2013.

[18] S. Nag, "Satellite Constellation Mission Design using Model-Based Systems Engineering and Observing System Simulation Experiments," *Small Satellite Conference*, 2014.

[19] S. Nag, C. Gatebe, D. W. Miller, O. L. De Weck, "Effect of Satellite Formation Architectures and Imaging Modes on Albedo Estimation of major Biomes," *Acta Astronaut.*, 2015.

[20] S. Nag, "Collaborative Competition for Crowdsourcing Spaceflight Software and STEM Education using SPHERES Zero Robotics," Massachusetts Institute of Technology, 2012.

[21] NASA ARC, "Small Spacecraft Technology State of the Art," NASA/TP–2014–216648/REV1, 2014.

[22] J. Esper, et al, "Leonardo-BRDF: A New Generation Satellite Constellation," presented at the International Astronautical Conference, Rio de Janeiro, Brazil, 2000.

[23] A. Marinan, et al "Ad hoc CubeSat constellations: Secondary launch coverage and distribution," in *2013 IEEE Aerospace*.

[24] S. Nag, J. LeMoigne, and O. L. De Weck, "Cost and Risk Analysis of Small Satellite Constellations for Earth Observation," in *IEEEAerospace Conference 2014*, Big Sky

[25] William Blackwell et al, "Nanosatellite for Earth Environmental Monitoring: The MICROMAS Project," presented at the Interplanetary CubeSat Workshop 2012.

[26] C. M. Pong, et al, "One-Arcsecond Line-of-Sight Pointing Control on Exoplanetsat, a Three-Unit CubeSat," *Adv. Astronaut. Sci.*, vol. 141, pp. 147–166, 2011.

[27] C. W. Crowell, "Development and analysis of a small satellite attitude determination and control system testbed," Massachusetts Institute of Technology, 2011.

[28] A. Schwarzenberg-Czerny, et al, "The BRITE Nanosatellite Constellation Mission," *COSPAR Scientific Assembly*, 2010,

[29] N. Orr, et al, "Precision formation flight: the CanX-4 and CanX-5 dual nanosatellite mission," Small Sat, Utah 2007.

[30] D. A. Vallado, *Fundamentals of astrodynamics and applications*, Springer Science & Business Media, 2001.

[31] T. N. Edelbaum, "Optimum low-thrust rendezvous and station keeping," *AIAA J.*, vol. 2, no. 7, pp. 1196–1201, 1964.

[32] T. N. Edelbaum, "Optimum power-limited orbit transfer in strong gravity fields," *AIAA J.*, vol. 3, no. 5, 1965.

[33] E. D. Wise, "Design, analysis, and testing of a precision guidance, navigation, and control system for a dual-spinning Cubesat," Massachusetts Institute of Technology, 2013.

[34] J. R. Wertz, D. F. Everett, and J. J. Puschell, *Space Mission Engineering:The New SMAD*, First. Microcosm Press, 2011.

[35] T. J. Lang, W. S. Adams, "A comparison of satellite constellations for continuous global coverage," in *Mission Design & Implementation of Satellite Constellations* 1998.

[36] B. V. Oaida, et al, "Optical link design and validation testing of the Optical Payload for Lasercomm Science (OPALS) system," in *SPIE LASE*, 2014, p. 89710U–89710U.

[37] S. Janson and R. Welle, "The NASA Optical Communication and Sensor Demonstration Program," 2013.

[38] R. Hodges, et al, "ISARA – Integrated Solar Array and Reflectarray Mission Overview," Small Sat, Utah 2013.

[39] J. Sauder, et al "Ultra-Compact Ka-Band Parabolic Deployable Antenna for CubeSats," 4th Interplanetary CubeSat Workshop, London, United Kingdom, 2015.

[40] R. Kingsbury, K. Riesing, and K. Cahoy, "Design of a Free-Space Optical Communication Module for Small Satellites," Small Sat, Utah 2014

[41] B. Yost, "EDSN-Edison Demonstration for SmallSat Networks Overview," Small Sat, Utah 2013.

[42] M. Lin, T. Flatley, A. Geist, and D. Petrick, "NASA GSFC Development of the SpaceCube MINI," 2011.

[43] S. Chien, et al "Onboard processing and autonomous operations on the IPEX Cubesat," in *4th Annual Government Forum on CubeSats (GFC), Maryland, April 16, 2012.*, 2012.

[44] E. Razzano, M. Pastena, "A Novel AOCS Cold-Gas Micro-Propulsion System Design & Applications to Micro and Nano Satellites," *Small Sat Missions for Earth Observation*, 2010.

[45] P. Lozano, D. Courtney, "On the development of high specific impulse electric propulsion thrusters for small satellites," in *4S Symposium,* Portugal, 2010.

[46] J. Arlas, S. Spangelo, "GPS results for the radio aurora explorer II cubesat mission," *AIAA Student Conference,* 2012.

[47] F. J. Franquiz, P. Edwards, B. Udrea, M. V. Nayak, and T. Pueschl, "Attitude Determination and Control System Design for a 6U CubeSat for Proximity Operations and Rendezvous."

[48] J. C. Springmann, et al, "Magnetic sensor calibration and residual dipole characterization for application to nanosatellites," AIAA/AAS Astrodynamics Conf. 2010.

[49] J. Andrews, "Spaceflight Secondary Payload System (SSPS) and SHERPA Tug-A New Business Model for Secondary and Hosted Payloads," Small Sat, Utah 2012

[50] R. Rose, et al, "Nanosat Technology And Managed Risk; An Update Of The CYGNSS Microsatellite Constellation Mission Development," Small Sat, Utah 2014.

[51] S. Nag, C. K. Gatebe, and O. L. De Weck, "Observing System Simulations for Small Satellite Clusters estimating Bi-Directional Reflectance," *Int. J. Appl. Earth Obs. Geoinformation*, 2015.

[52] J. Stupl, et al, "LightForce Photon-Pressure Collision Avoidance: Updated Efficiency Analysis Utilizing a Highly Parallel Simulation Approach," Advanced Maui Optical and Space Surveillance Technologies Conference, 2014.

BIOGRAPHIES

Sreeja Nag is a PhD candidate in Space Systems Engineering at the Massachusetts Institute of Technology and a part-time research engineer at NASA Ames Research Center. She has a dual SM in Aeronautics & Astronautics Engineering along with Technology & Policy at MIT. She has worked at NASA Goddard Space Flight Center, has summer research experience with NASA JPL in 2008, the European Space Agency (ESTEC) in 2010 and led the SPHERES Zero Robotics Program in 2011. Email: sreeja_n@mit.edu
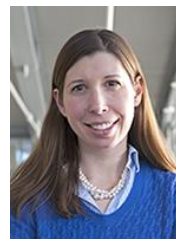
Kerri Cahoy received a B.S. in Electrical Engineering from Cornell University in 2000, an M.S. in Electrical Engineering from Stanford University in 2002, and a Ph.D. in Electrical Engineering from Stanford University in 2008. After working as a Senior Payload and Communication Sciences Engineer at Space Systems Loral, she completed a NASA Postdoctoral Program Fellowship at NASA Ames Research Center and held a research staff appointment with MIT/NASA Goddard Space Flight Center. She is currently a Assistant Professor in the MIT Department of Aeronautics and Astronautics with a joint appointment in the Department of Earth and Planetary Sciences at MIT. Email: kcahoy@mit.edu

Olivier de Weck is a Professor of Aeronautics and Astronautics and Engineering Systems at the Massachusetts Institute of Technology. He is the Executive Director of MIT Production in the Innovation Economy (PIE) Study and the Director, Center for Complex Engineering Systems at KACST and MIT. Email: deweck@mit.edu